Lithospheric deformation due to the 2015 M7.2 Sarez (Pamir) earthquake constrained by 5 years of space geodetic observations

Zeyu Jin[1], Yuri Fialko[1], Alexander Zubovich[2], Tilo Schöne[3]

[1]Institute of Geophysics and Planetary Physics, Scripps Institution of Oceanography, University of California San Diego, La Jolla, CA 92093, USA.
[2]Central-Asian Institute for Applied Geosciences, Bishkek, 720027, Kyrgyz Republic.
[3]Helmholtz Centre Potsdam GFZ, German Research Centre for Geosciences, 14473 Potsdam, Germany.

fig:un

Key Points:

- We present geodetic observations of coseismic and postseismic deformation due to the 2015 M_w7.2 Sarez (Pamir) earthquake.
- Near-field postseismic deformation is dominated by shallow afterslip and possibly poroelastic relaxation at the NE end of the earthquake rupture.
- Data do not show a clear signal expected of viscoelastic relaxation, indicating effective viscosity of the lower crust $> 10^{19}$ Pa s.
- We investigate triggering relationships between the M7.2 earthquake and a pair of M6+ events that occurred within 1 year and 100 km of the mainshock.

Corresponding author: Zeyu Jin, zej011@ucsd.edu

Abstract
The 2015 M7.2 Sarez (Pamir) earthquake occurred at the north-west margin of the Tibetan Plateau. We use Sentinel-1 and ALOS-2 Synthetic Aperture Radar and Global Navigation Satellite System data to investigate coseismic and postseismic deformation due to the Sarez earthquake. Kinematic inversions show that the earthquake ruptured a ∼80 km long, sub-vertical fault producing the maximum surface offset of 3-4 meters on the south-west and central fault segments. In contrast, the largest postseismic displacements are observed at the north-east end of the earthquake rupture, predominantly on the west (hanging wall) side of the fault with an average rate of 20-30 mm/yr in the satellite line of sight. We use the derived coseismic and postseismic slip models to investigate mechanisms of time-dependent relaxation, stress transfer and possible triggering relationships between the Sarez earthquake and a sequence of strong M6+ events that occurred within ∼100 km of the 2015 earthquake. We find that the near-field postseismic displacements are best explained by shallow afterslip driven by the coseismic stress changes. The data also allow some contribution from poroelastic rebound, but do not show a clear signature of viscoelastic relaxation in the lower crust and upper mantle during the observation period, suggesting a lower bound on the effective viscosity of $\sim 10^{19}$ Pa s. A pair of M6+ events that occurred within 100 km and several months of the 2015 mainshock have experienced near-zero and in some cases negative static Coulomb stress changes, suggesting either delayed dynamic triggering, or no relation to the mainshock.

Plain Language Summary

Large earthquakes are often followed by slow deformation that results from redistribution and relaxation of coseismic stress changes in the host rocks. The patterns and rates of postseismic deformation can be used to learn about the properties of rocks at depth. We analyzed surface deformation that occurred during and after a major (magnitude 7.2) earthquake that occurred in the Pamir orogen at the north-west margin of Tibet. We used radar imagery from satellites of the European and Japanese space agencies, as well as data from the Global Navigational Satellite System to measure subtle (centimeter-scale) displacements of the Earth's surface that occurred within 100 km from the earthquake epicenter. A combination of coseismic and postseismic displacement data reveals that the earthquake rupture split into two branches as it was propagating from south-west to north-east. We found evidence of slow aseismic creep ("afterslip") at the north-east end of the earthquake rupture. In contrast, we do not observe a broad pattern of displacements expected from enhanced viscous flow in the lower crust and/or upper mantle. The lack of the respective signal argues for a relatively strong "ductile" portion of the Tibetan lithosphere.

Introduction

The Pamir orogen, situated at the north-west edge of the Tibetan Plateau, is a result of collision due to the ongoing northward impingement of the Indian continent into Eurasia (Figure 1). The Pamir thrust system (PTS), located at the northern margin of the orogen, accommodates $\sim 13 - 19$ mm/yr of the Indian-Eurasia convergence, as indicated by the GNSS observations (e.g., Zubovich et al., 2010; Ischuk et al., 2013; Zubovich et al., 2016). This is about one half of the total convergence rate between the Indian and the Eurasian plates at this longitude (~ 34 mm/yr), which makes the Pamir thrust system one of the fastest deforming regions in the entire India-Asia collision zone. Much of the observed seismicity is associated with the frontal thrust system (e.g., Storchak et al., 2013; Schurr et al., 2014), but active faulting is also observed in the Pamir interior (e.g., Mechie et al., 2012; Sippl et al., 2013; Kufner et al., 2017). The most recent major earthquake, the Dec. 2015 M_w7.2 Sarez event, ruptured the Sarez-Karakul fault system (SKFS) consisting of left-lateral faults that accommodate the north-south shortening and east-west extension in the Pamir interior (Schurr et al., 2014). A penultimate major event on the SKFS occurred

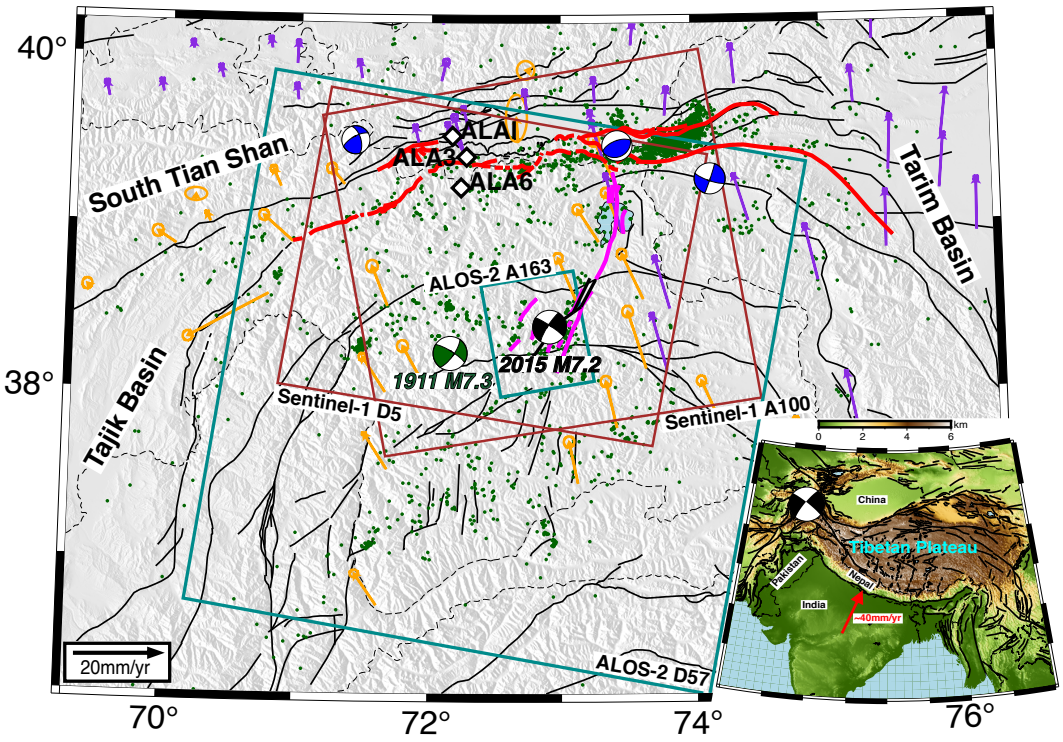

Figure 1. Tectonic setting of the central Pamir region. Thin black lines denote presumed active faults (Mohadjer et al., 2016). Thick black lines and the black-and-white "beach ball" denote the surface trace and the focal mechanism of the 2015 M7.2 Sarez earthquake, respectively. The colored "beach balls" indicate the locations and focal mechanisms of the 1911 M_w7.2 earthquake (green), and M6+ events (blue) that occurred after the 2015 mainshock. Dark green dots denote seismicity within the top 30 km of the Earth's crust over the time period 2008-2010 (Schurr et al., 2014). Violet and orange arrows denote GNSS-determined velocities in a stable Eurasia reference frame (Zubovich et al., 2010; Ischuk et al., 2013, respectively). Color rectangles denote swathes of SAR data from Sentinel-1 (brown) and ALOS-2 (teal) missions used in this study. Magenta lines denote faults of the Sarez-Karakul fault system (SKFS), and red lines denote faults of the Pamir thrust system (PTS). White diamonds denote three continuous GNSS sites used in this study. (Inset) A regional view and topography of the India-Eurasia collision zone.

in 1911 and also ruptured a sinistral fault with a geometry similar to that of the 2015 event (Kulikova et al., 2016). Both earthquakes highlight the importance of the NE-trending SKFS in the central Pamir. Within two years following the 2015 mainshock, a series of $M_w > 6$ earthquakes occurred on the east-west trending fault systems immediately to the north of the SKFS (e.g., He, Hetland, et al., 2018; He, Ding, & Xu, 2018). This clustering of large earthquakes raises questions about possible mechanisms of time-dependent stress transfer and earthquake triggering.

Several previous studies investigated the 2015 Sarez earthquake from geological, geodetic and seismic perspectives (e.g., Sangha et al., 2017; Metzger et al., 2017; Elliott et al., 2020). These studies showed that the Sarez earthquake ruptured a system of sinistral subvertical faults with maximum slip up to $\sim$ 4 m on the southern and central segments of the earthquake rupture (Sangha et al., 2017; Metzger et al., 2017). Slip models based on inversions of geodetic data suffered from lack of the near-field coverage due to challenging surface conditions such as the rugged topography, snow cover and near-fault damage causing

decorrelation of the radar phase, which made it difficult to constrain the details of coseismic slip distribution in the shallow crust (e.g., Sangha et al., 2017; Metzger et al., 2017). Elliott et al. (2020) presented a map of surface ruptures using Landsat-8 optical imagery, although their coseismic pairs used images acquired more than one year after the earthquake, which, as we demonstrate below, include a non-negligible contribution of postseismic displacements. The latter are of primary interest for this study.

In this paper, we investigate time-dependent deformation that occurred during ~ 5 years following the 2015 mainshock. We first refine existing coseismic slip models by inverting line-of-sight (LOS) and pixel offset data (which provide a better near-fault coverage) from the Sentinel-1 and ALOS-2 Interferometric Synthetic Aperture Radar (InSAR) missions. The respective slip model is then used as an initial condition in simulations assuming various time-dependent mechanisms such as afterslip, viscoelastic, and poroelastic relaxation. The model predictions are compared to the time-series of LOS displacements obtained from Sentinel-1 data and GNSS positions from a local continuously recording network, to place constraints on the mechanical properties of continental lithosphere in a collision zone between the Indian and Eurasian plates. Finally, we apply best-fit coseismic and postseismic models to investigate possible triggering by the Sarez earthquake of a pair of M6+ events that occurred to the NE of the mainshock.

1 Coseismic Deformation

The epicentral area of the 2015 Sarez earthquake is well imaged by several SAR missions including Sentinel-1 and ALOS-2. Because the Pamir interior is a remote area with high elevation and rugged topography, GNSS observations are limited. The closest continuously recording sites are located along the Pamir thrust system that is further than 100 km from the earthquake epicenter. Therefore we mostly rely on the SAR data to constrain finite fault models of the 2015 earthquake.

1.1 Coseismic SAR Data

The SAR data used in this study (Figures 1 and 2) include two Sentinel-1A tracks (ascending track 100 and descending track 5), and two ALOS-2 tracks (descending track 57 and ascending track 163, acquired in ScanSAR and Stripmap modes, respectively). All interferometric pairs were processed using GMTSAR, an open source InSAR processing package based on Generic Mapping Tools (Sandwell et al., 2011). Topography contributions to the radar phase were removed using the SRTM digital elevation model (Farr et al., 2007).

The C-band (radar wavelength of 55 mm) Sentinel-1 data are susceptible to decorrelation under challenging surface conditions such as those in the study area, resulting in loss of data and unwrapping errors (Ahmed et al., 2011). Phase unwrapping is particularly challenging near the rupture trace due to large phase gradients and changes in the backscatter characteristics of the ground caused by off-fault damage. To maximize the near-field data coverage, we multi-looked the focused SAR data using a 400 m-wide Gaussian filter, and experimented with the width of an adaptive filter prior to phase unwrapping (Goldstein & Werner, 1998), and thresholds for admissible phase discontinuity (DEFOMAX parameter used in SNAPHU, Statistical-cost Network-flow Algorithm for Phase Unwrapping, (C. Chen & Zebker, 2002)). In particular, we systematically varied the phase discontinuity parameter and picked a value that rendered the smoothest unwrapped phase within ~ 10 km from the earthquake rupture. We then manually masked out obvious unwrapping errors. The performance of our phase unwrapping strategy was evaluated using a preliminary coseismic slip model derived from inversions of other available data (i.e., excluding an interferogram that is being tested). Figures 2 and S2,3 illustrate improvements in the near-field data coverage.

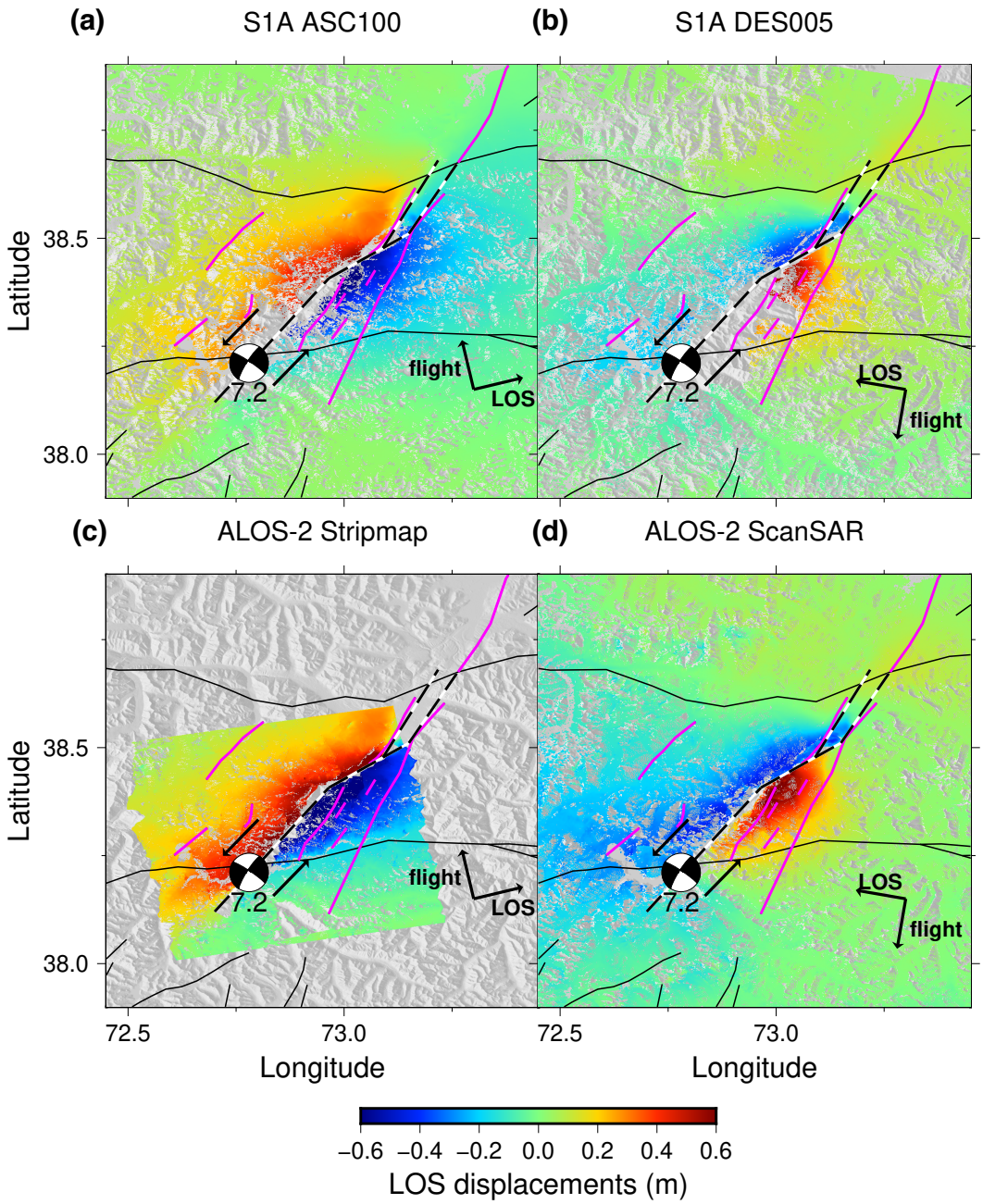

Figure 2. LOS displacements from (a,b) Sentinel-1 and (c,d) ALOS-2 interferograms. Motion toward the satellite is deemed positive. The magenta lines denote faults of the SKFS, and thin curvy black lines denote other presumed active faults (Mohadjer et al., 2016). The black-and-white dashed lines denote the modeled trace of the 2015 M7.2 earthquake. Black arrows show the satellite heading and the line of sight direction.

The ALOS-2 L-band (wavelength of 236 mm) data typically suffer less decorrelation compared to the C-band data. However, the L-band data may be more strongly affected by the ionospheric artifacts (Rosen et al., 2010; Meyer & Nicoll, 2008). We applied the split-spectrum method (Gomba et al., 2015; Fattahi et al., 2017) to reduce the ionospheric contributions to the ALOS-2 ScanSAR phase (Figure S4). We then unwrapped the residual interferograms to calculate the LOS displacements.

High-quality SAR data from more than two look directions are necessary to fully characterize surface displacements due to large shallow earthquakes (e.g., Fialko et al., 2001). To complement the LOS displacements from the ascending and descending satellite orbits, we computed the range and azimuth offsets from the Sentinel-1 data. The pixel offset data were found to have a low signal-to-noise ratio (SNR, see Figure S10) and therefore were not used in inverse modeling. However, the pixel offset data proved useful for identifying a displacement discontinuity associated with the rupture trace (Figure S5). Finally, we used the along-track interferometry (ATI), a high-resolution phase measurement equivalent to the azimuth offsets (e.g., Bechor & Zebker, 2006; Barbot, Hamiel, & Fialko, 2008). It exploits a parallax effect to measure surface displacements in the azimuthal (along-track) direction. To reduce speckle, we filtered the ATI phase using a 500 m-wide Gaussian filter.

1.2 Inversions of Coseismic Displacement Data

A wide-swath capability of the Sentinel-1A and ALOS-2 missions ensures that interferograms extend into areas where coseismic displacements are negligible. Because phase unwrapping is subject to phase ambiguity, we resolved the latter by adding or subtracting a multiple of 2π that minimizes the root mean square (RMS) of the far-field data. We then combined conventional and along-track interferograms in joint inversions for the coseismic slip model.

Each coseismic scene was sub-sampled using an iterative quad-tree algorithm (K. Wang & Fialko, 2015). Given the patch size of ~ 1 km in the shallowest part of the slip model, we sampled the near-field data with a minimum size of discretization cells of about 250 to 300 m. The unit look vectors were computed by averaging the original values in the same discretization cells as used for sub-sampling the phase data.

The rupture trace was digitized based on the SAR offset (Figure S1) and field survey data (e.g., Schurr et al., 2014; Metzger et al., 2017). Figure S5 shows the respective fault traces. The northern end of the earthquake rupture exhibits some complexity. In particular, the displacement discontinuities estimated from different offset maps do not coincide, presumably due to rupture bifurcation and buried slip. We interpret these observations as indicating two fault branches, a western branch (labeled F1 in Figure S5) which did not break the surface coseismically, and an eastern branch (labeled F2 in Figure S5) that did. The L-band ALOS-2 phase data that are less affected by decorrelation lend support to this interpretation; in particular, one can see a clear phase discontinuity across the eastern branch, and a high phase gradient across the western branch (Figure S6). The F1 branch is in agreement with rupture models proposed by Sangha et al. (2017); Metzger et al. (2017), and the F2 branch was suggested by Elliott et al. (2020) based on the geologically mapped fault scarps and cross-correlation of the optical Landsat-8 imagery. We propose that both branches were activated during the 2015 event. Furthermore, below we show that the buried coseismic slip on the western (F1) branch of the earthquake rupture is required by postseismic observations of shallow afterslip.

We approximated the mapped fault trace by a set of rectangular segments (denoted by dark gray and red lines in Figures S5 and S6, respectively). The subsurface geometry of the SKFS is not well-known due to low background seismicity and a sparse seismic network that is unable to provide accurate aftershock locations. We extended the rectangular segments approximating the fault geometry to the depth of 25 km, and by several kilometers beyond the mapped fault traces along the fault strike. Each segment was then divided

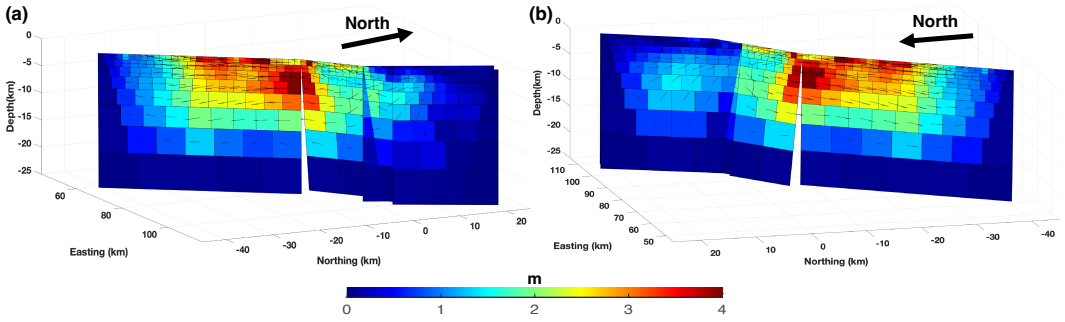

Figure 3. Slip distribution from the joint inversion of space geodetic data assuming a elastic-half space model. Colors denote the total amplitude of slip, and arrows show the direction of slip. The two panels (a,b) represent perspectives from different vantage points.

into patches which sizes increase with depth in a geometric progression to ensure that the model resolution matrix remains nearly diagonal (Fialko, 2004b). We computed Green's functions for the strike and dip components of slip on each patch at every sub-sampled observation point. We applied positivity constraints to strike-slip components, such that no slip was allowed to be right-lateral. No positivity constraints were imposed on the dip-slip components. The first-order Tikhonov regularization (Golub et al., 1999) was applied to avoid extreme variations in slip between the adjacent fault patches, including patches at the boundaries between fault segments. We further imposed a "soft" zero-slip boundary conditions at the fault edges, except at the Earth's surface (Jin & Fialko, 2020).

We performed two sets of inversions, one using Green's function for a homogeneous elastic half-space (Okada, 1985) and another for a layered elastic half space (R. Wang et al., 2003). For the latter, we estimated the depth distribution of elastic moduli from the 2D seismic tomography models of the central Pamir (Mechie et al., 2012). Due to the sparse distribution of seismic stations, the inferred 1-D seismic velocity profile (Figure S7) shows little variation in elastic moduli above 28 km, i.e., over the entire depth extent of the modeled fault. As a result, slip models assuming a layered half space (3) are not noticeably different from those assuming a homogeneous elastic half-space ().

1.3 Best-fit Coseismic Models

Figures 4 and S9 show the sub-sampled data, predictions of the best-fit models, and residuals (data minus model predictions) for all of the data used in the inversions. Overall, the model fits the main features of the displacement field well, with the variance reduction of more than 96% for the conventional interferograms and 85% for the ATI. We did not incorporate the Sentinel-1A range offsets into the inversion because the offset data at the south-west end of the rupture are very noisy (Figure S10). Most of the data misfits are concentrated near the south-west end of the fault, where

(e.g., Lohman & Simons, 2005).

Figures 3 and S8 show the slip distribution for the best-fit models, assuming the elastic half-spaces, respectively. All fault segments are sub-vertical and the sense of slip is mostly left-lateral at the south-west and central parts of the rupture. An appreciable dip-slip component is inferred at the north-east part of the rupture. The largest slip is concentrated at the center of the south-west fault segment, with an amplitude of 3-4 meters at, or close to, the Earth's surface. In contrast, the north-east fault segment produced either small (branch F2, see Figure S6) or no (F1) surface offset (e.g., Metzger et al., 2017; Elliott et

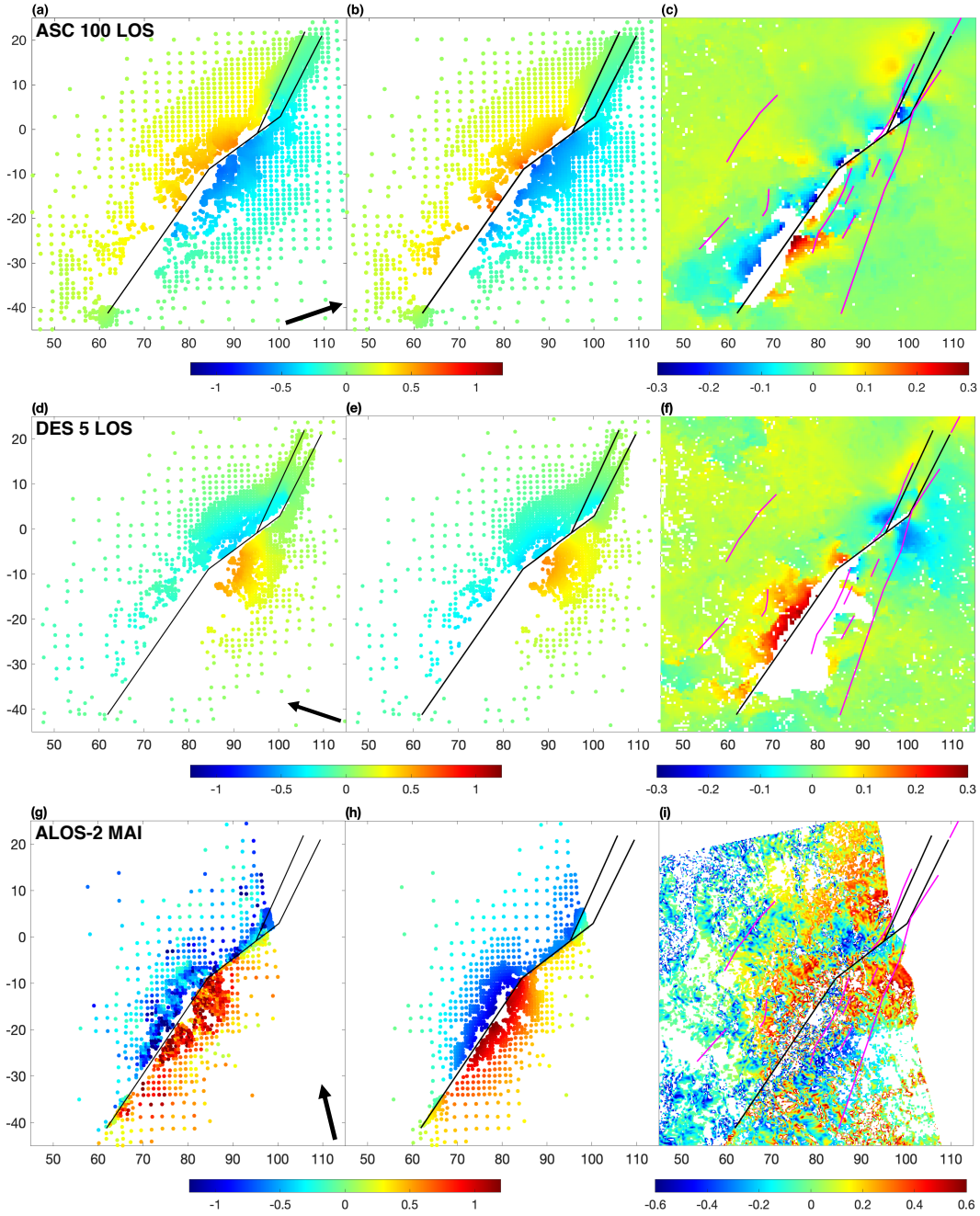

Figure 4. Coseismic (a,d,g) sub-sampled data, (b,e,h) best-fitting models, and (c,f,h) residuals for the Sentinel-1 LOS displacement data from ascending track 100 (top row), descending track 5 (middle row), and ALOS-2 along-track interferogram (bottom row). Color denotes the amplitude of LOS or along-track displacements, in meters. Black arrows show the projection directions. Magenta lines denote the SKFS faults, and black lines denote the modeled trace of the 2015 rupture. Horizontal and vertical axes are in UTM coordinates (easting and northings, respectively) in kilometers, with respect to a local origin (72°E, 38.5°N).

al., 2020). Below we argue that such a behavior may be controlled by local lithological conditions (Bullock et al., 2014).

The "geodetic" moment computed from the best-fit slip model, assuming . This corresponds to a moment magnitude of , in a good agreement with the seismic moment magnitude of 7.2 (USGS, 2015). Such an agreement is similar to findings from previous studies of major earthquakes for which high-quality space geodetic data are available (e.g., Simons et al., 2002; Fialko, 2004b; Fialko et al., 2005; Barbot, Hamiel, & Fialko, 2008; Jin & Fialko, 2020).

2 Postseismic Deformation

To study postseismic deformation due to the 2015 Sarez earthquake, we processed and analyzed all InSAR data collected by the Sentinel-1 and ALOS-2 satellites over a time period of 5 years following the earthquake. Data are available from the Sentinel-1A ascending track 100 and descending track 5, and ALOS-2 descending track 57 acquired in the ScanSAR mode. We also use data from three permanent GNSS sites (ALAI, ALA3 and ALA6) of the Alai GNSS network located in the Alai Valley, ∼120-150 km to the northwest from the epicenter of Sarez earthquake (Figure 1).

2.1 Analysis of Postseismic Timeseries

Sentinel-1 data were processed using GMTSAR (Sandwell et al., 2011). We geometrically aligned a single reference image (approximately in the middle of the ∼ 5-year-long time interval of postseismic acquisitions) to the rest of the images, and formed interferometric pairs between the first post-earthquake acquisition and all subsequent acquisitions. Persistent scatterers common to all interferograms were identified using StaMPS package (Hooper & Zebker, 2007). To check for the 2π phase ambiguity, we generated closed circuits of interferograms, and computed phase residuals. The latter were found to be on the order of 10^{-5} radians. Atmospheric artifacts were suppressed using a common scene stacking method (Tymofyeyeva & Fialko, 2015).

Figure 5 shows the cumulative postseismic LOS displacements from the two Sentinel-1 tracks covering the epicentral area, about 5 years after the earthquake. The data reveal a sharp step in the LOS displacements across the western branch (F1, see Figure 7a) of the NE segment of the earthquake rupture in the ascending track, with the maximum amplitude up to ∼ 80 mm. Such a discontinuity in the LOS displacements is not correlated with topography (compare green and black dots in Figure 7b), and likely represents afterslip at the NE end of the earthquake rupture. The LOS displacement signal in the descending track is much smaller (see Figures 5b and 7b); note that given the SW-NE fault orientation, the LOS projection of strike-slip motion is almost zero for the descending track. There is no step or high gradient in the LOS displacements across the eastern fault branch (F2, Figure 7b). Figure 6 shows the time-series of LOS displacements at several locations across the fault trace where the anomalous displacements are detected. All six postseismic time-series show a gradually decelerating transient, consistent with afterslip on the fault segment F1. The data also reveal an accelerated deformation event in 2019 (e.g., see Figure 6b). We further discuss this event in the Discussion section.

To verify results shown in Figures 5-7, we processed ALOS-2 data acquired over the same time period. ALOS-2 acquisition dates are listed in Table S1 in the Supporting Information. Because the temporal resolution of ALOS-2 data is limited due to large and irregular revisit times and changes in acquisitions modes, we generated 14 independent (i.e., not sharing a common acquisition) interferograms that were subsequently stacked to enhance the signal (Figure S13b). Figure 7 shows the resulting average LOS velocities across the NE part of the earthquake rupture. Sentinel-1 and ALOS-2 data (Figure S13) have similar lines of sight and incidence angles, and both show the same features around the

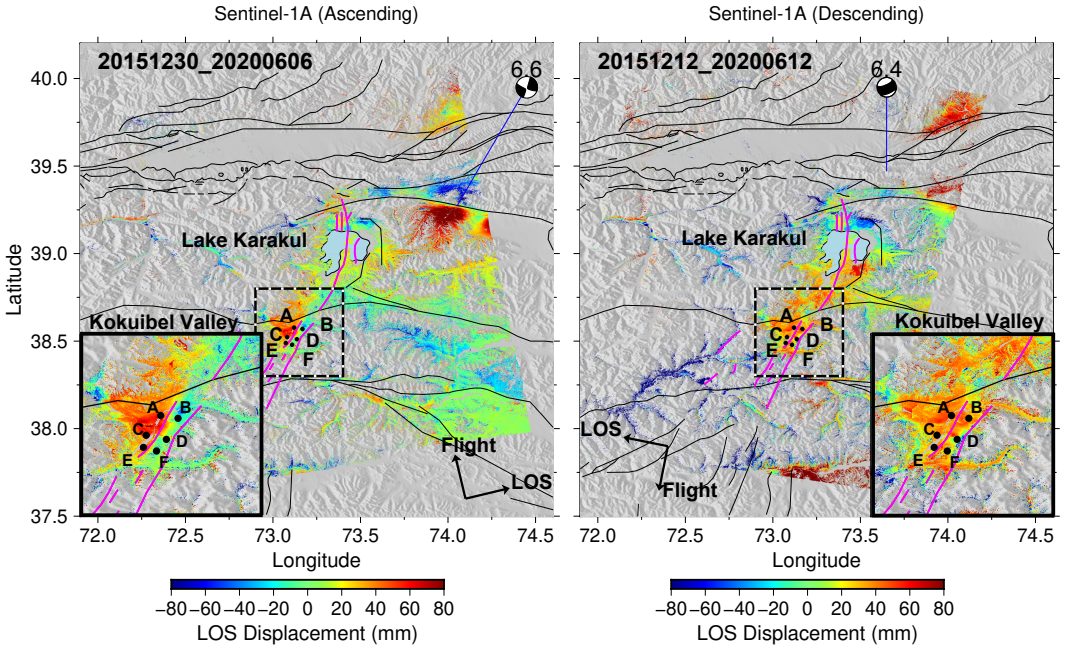

Figure 5. Cumulative Sentinel-1 LOS displacements spanning ∼ 5 years following the mainshock from (a) ascending track 100, and (b) descending track 5. Positive LOS displacements correspond to surface motion towards the satellite. Observation periods are indicated in the top left corner of each panel. The time series of LOS displacements between pair of points "A-B", "C-D" and "E-F" are shown in Figure 6. Magenta lines denote the SKFS faults. (Insets) Close-up views of postseismic LOS displacements in the Kokuibel Valley area outlined by the dashed rectangle.

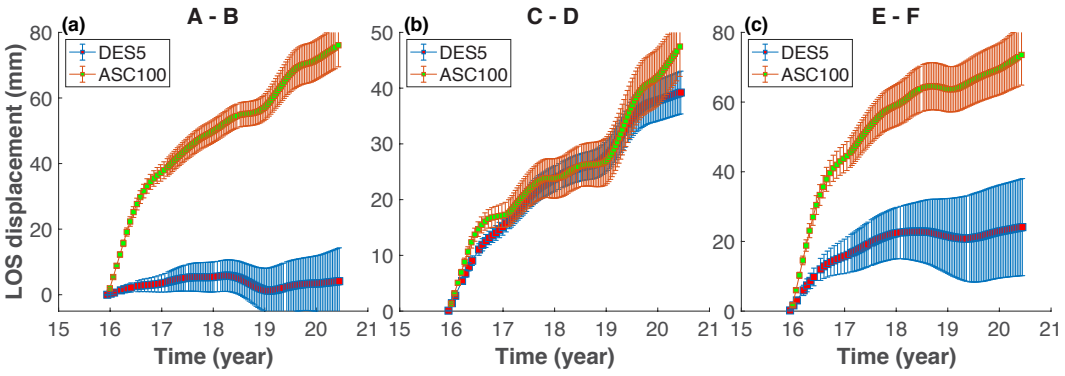

Figure 6. LOS displacement time series of relative displacements between the closely-spaced pairs of points (a) A-B, (b) C-D, and (c) E-F spanning the fault trace (see Figure 5). Red dots denote the LOS displacements from the descending track, and green dots denote the LOS displacements from the ascending track. Error bars represent the standard deviation of LOS displacements for persistent scatters within 500 m from the reference points.

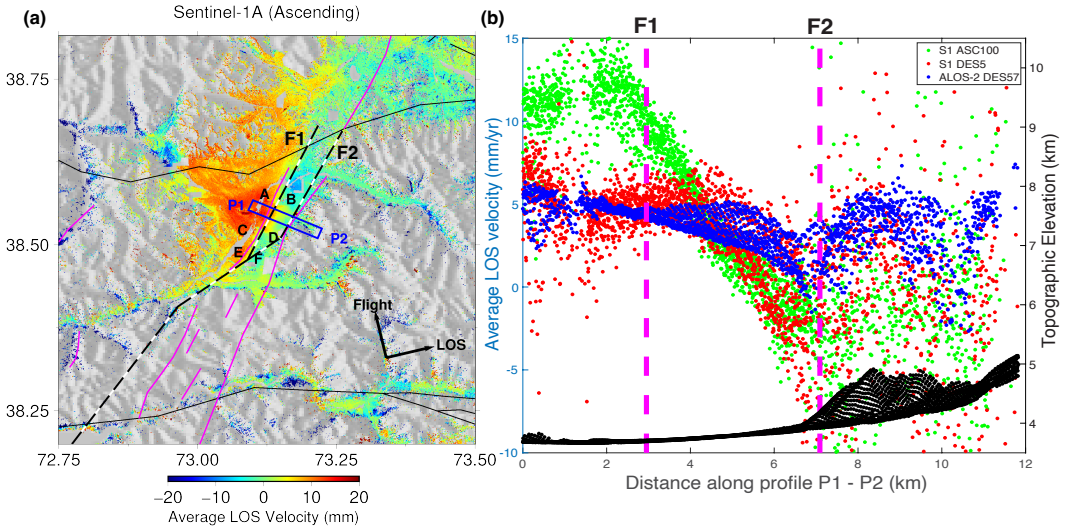

Figure 7. (a) A detailed map of Sentinel-1 LOS velocity from the ascending track, averaged over 5 years following the 2015 earthquake. Other notation is the same as in Figure 2. F1 and F2 denote the two sub-parallel fault branches at the NE end of the earthquake rupture. A blue rectangle indicates a profile shown in panel (b). (b) A comparison of Sentinel-1 and ALOS-2 average LOS velocities from a profile denoted by a blue rectangle in panel (a). Black dots denote variations in topography along the same profile.

fault segments F1 and F2. In particular, the two independent data sets from the descending orbits show gradual variations in the LOS velocity across both fault segments, but high gradients across segment F1 in the ascending interferograms, with positive LOS velocities on the western side of the fault trace. The LOS velocity gradients follow the fault strike, and seem to extend further to the NE into the Lake Karakul (Figures 5a and 7a).

InSAR observations were complemented by GNSS data from three continuous sites closest to the 2015 earthquake rupture, ALAI, ALA3, and ALA6 (Figure 1). Daily solutions were obtained using GAMIT/GLOBK software (Herring et al., 2016). Subsequently, we calculated position time series for all stations of the network in the Eurasian reference frame, for a time period of 6 years from 2014/00/01 to 2020/06/30.

3 Modeling of Postseismic Deformation

In this section we use a combination of forward and inverse models to evaluate possible contributions of various postseismic deformation processes (afterslip, poroelastic, and viscoelastic relaxation), and compare them to the displacement timeseries obtained from InSAR and GNSS measurements.

3.1 Afterslip

The spatio-temporal pattern of near-fault postseismic displacements, including high displacement gradients across the fault trace, and the same sense of coseismic and postseismic LOS displacements, suggest that the observed near-field deformation transient (Figures 3-5) involves afterslip on the earthquake fault. We test this hypothesis using both kinematic and dynamic (i.e., stress-driven) models, as described below.

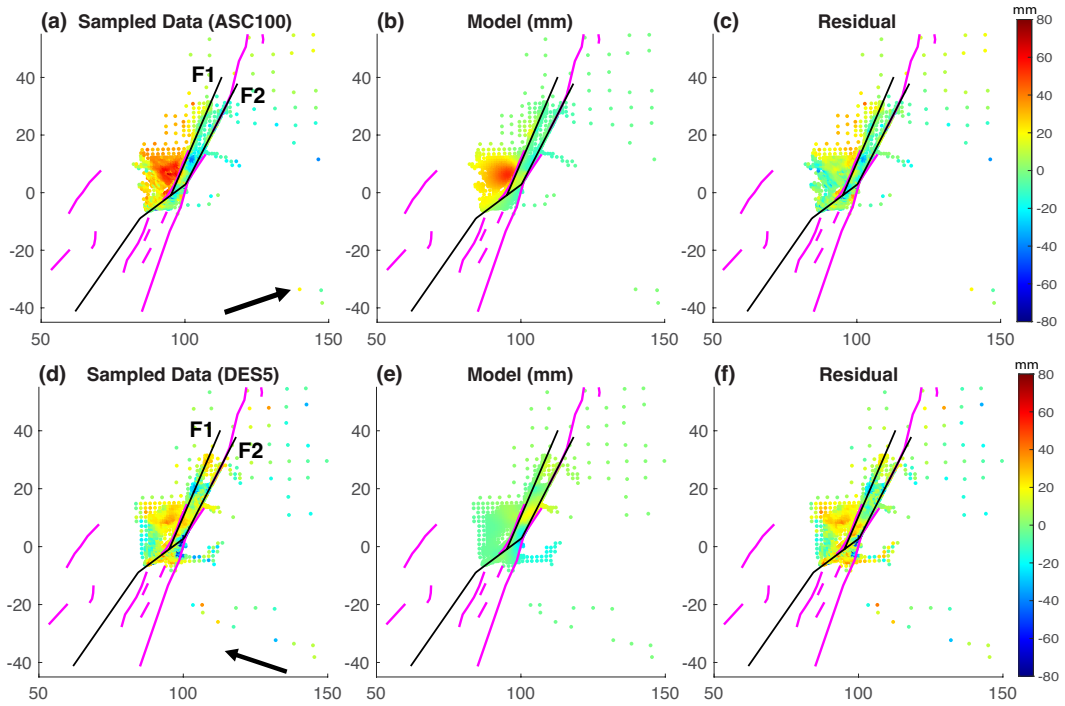

Figure 8. (a,d) Resampled postseismic cumulative surface displacements, (b,e) kinematic model predictions, and (c,f) residuals for the Sentinel-1 ascending track 100 (top row) and descending track 5 (bottom row). Color denotes the amplitude of LOS displacements in millimeters. Black arrows denote the look vectors. Other notation is the same as in Figure 7.

3.1.1 Kinematic Inversions

Assuming that the observed near-field postseismic displacements are dominated by afterslip, we invert them for the best-fitting slip distribution on a fault, using the fault geometry described in Section "Inversions of Coseismic Displacement Data", extended in both strike and dip directions. Because postseismic InSAR data remain coherent primarily over the NE section of the earthquake rupture, we focus on the respective part of the fault in our inversions. The data are LOS displacements from the ascending and descending orbits spanning ∼5 years after the mainshock (Figure 5). Data outside of the Kokuibel valley (Figure 5) are relatively noisy, and therefore masked out. The data are sampled using an adaptive quad-tree algorithm (K. Wang & Fialko, 2015). Figures S14 and 8 show the best fitting afterslip models and a comparison between the data and model predictions, respectively. The kinematic afterslip model is able to explain most of the signal to the west of F1 segment seen in the ascending data (Figures 8a,b,c). Smaller but still positive LOS displacements apparent in the descending data in the same area are not well explained by the kinematic inverse models (Figures 8d,e,f). As we show below, a mismatch between the best-fitting afterslip model and data from the descending orbit may be indicative of poro-elastic deformation.

3.1.2 Stress-Driven Afterslip

Our kinematic inversions suggest that most of the observed near-field postseismic deformation during ∼ 5 years after the 2015 Sarez earthquake may be due to afterslip (Figures 8 and S14). To further investigate this possibility, and to evaluate in situ frictional properties of a fault section involved in afterslip, we performed forward simulations of afterslip con-

strained by time-dependent surface deformation data (e.g., Barbot, Fialko, & Bock, 2009; Lindsey & Fialko, 2016; K. Wang & Fialko, 2018). Such simulations ensure that the amount, time dependence, and distribution of afterslip are consistent with relaxation of coseismic stress changes on a fault plane governed by the rate and state friction laws (J. H. Dieterich, 1979). Simulations were performed using the Fourier domain fictitious body force code Relax (Barbot & Fialko, 2010b, 2010a). In these simulations, afterslip is allowed to occur on fault areas that experienced coseismic increases in the Coulomb stress (Barbot & Fialko, 2010b). The geometry of the fault is the same as the one used in kinematic inversions.

Because the observed near-fault displacements (see Figures 5-7) are orders of magnitude larger than the laboratory-derived values of the critical slip-weakening distance (J. Dieterich, 2015; Fialko, 2015), in our calculations we ignore the evolution effect and use a quasi-steady purely rate-strengthening constitutive law (e.g., Lapusta et al., 2000; Barbot, Fialko, & Bock, 2009), $V = 2V_0 \sinh[\Delta\tau/((a-b)\sigma)]$, where V_0 is the reference slip rate, $\Delta\tau$ is the driving Coulomb stress change, a and b are the rate and state parameters, and σ is the effective normal stress acting on a fault. Barbot, Fialko, and Bock (2009) assumed $b = 0$ (their eq. 11), which is a sufficient (although not a necessary) condition for a purely rate-dependent friction under velocity-strengthening conditions.

We assume that areas of high coseismic slip are velocity weakening and thus do not participate in postseismic creep. To allow afterslip in areas of overlap between seismic slip and afterslip, we truncated the coseismic model at 25% of the maximum slip amplitude. The remaining coseismic slip was multiplied by a constant to preserve the seismic moment (Barbot, Fialko, & Bock, 2009). Since most of coseismic slip at the NE end of the earthquake rupture occurred on the F1 segment (Figure 3), and afterslip occurred on both the F1 and F2 segments (Figures $5-7$), .

We performed forward calculations over a wide range of model parameters, including V_0 and $(a-b)\sigma$. Optimal values of these parameters that render the best agreement between model predictions and postseismic InSAR time-series are: $V_0 = 2 \times 10^{-2}$ m/yr, and $(a-b)\sigma = 7$ MPa. Assuming the effective normal stress on the fault $\sigma = 100$ MPa, the corresponding rate-and-state frictional parameter $a - b = 7 \times 10^{-2}$, which is on a high end of the experimentally measured values of $O(10^{-2})$ (e.g., Marone, 1998; Mitchell et al., 2013, 2016), and comparable to the values inferred from space geodetic studies of afterslip associated with other large crustal earthquakes (e.g., Barbot, Fialko, & Bock, 2009; Lindsey & Fialko, 2016; K. Wang & Fialko, 2018). Figure 9 shows the afterslip distribution on fault segments F1 and F2. As one can see from Figure 9, the highest amplitudes of afterslip are located on the periphery of high coseismic slip areas, as expected (e.g., K. Wang & Fialko, 2014, 2018). overall agreement between the model predictions and geodetic data (10), support a suggestion that shallow afterslip dominated the near-field postseismic deformation at the NE end of the earthquake rupture over the 5-yr period of observations.

Similar to the results of kinematic inversions, the stress-driven afterslip models best explain the LOS displacements from the ascending track (Figures 5a and 10a). The model fit is notably worse for data from the descending track (Figures 5b and 10d). Next, we test a hypothesis that the poor model fit to the descending data is due to a contribution from another mechanism, namely the poro-elastic rebound.

3.2 Poroelastic Rebound

Some poroelastic deformation is expected following an earthquake if the host rocks contain pore-fluids and the pore space is connected to allow fluid percolation (e.g., Nur & Mavko, 1972; Rice & Cleary, 1976; Fialko, 2004a; LaBonte et al., 2009). We evaluated a total response due to the poroelastic rebound by differencing models of coseismic displacements under fully drained and undrained conditions (e.g., Peltzer et al., 1998; Jonsson et al., 2003; Fialko, 2004a). We assumed that the poroelastic rebound was confined to the top 25 km of the crust and the drained and undrained values of the Poisson's ratio were 0.21 and

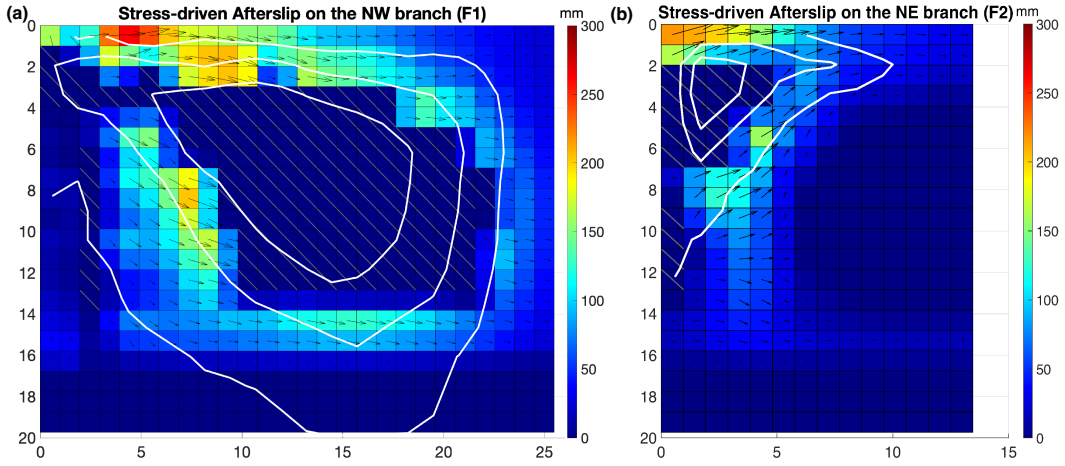

Figure 9. Cumulative afterslip from stress-driven afterslip simulations assuming a rate-strengthening fault friction. that experienced a coseismic decrease in the Coulomb stress. (a) Afterslip distribution on the F1 segment. (b) Afterslip distribution on the F2 segment (see Figure 7). Colors denote the amplitude of slip, in millimeters. Arrows denote slip direction for each slip patch. White contours denote the coseismic slip (see Figure 3) at 0.5 m intervals, starting at 0.5 m.

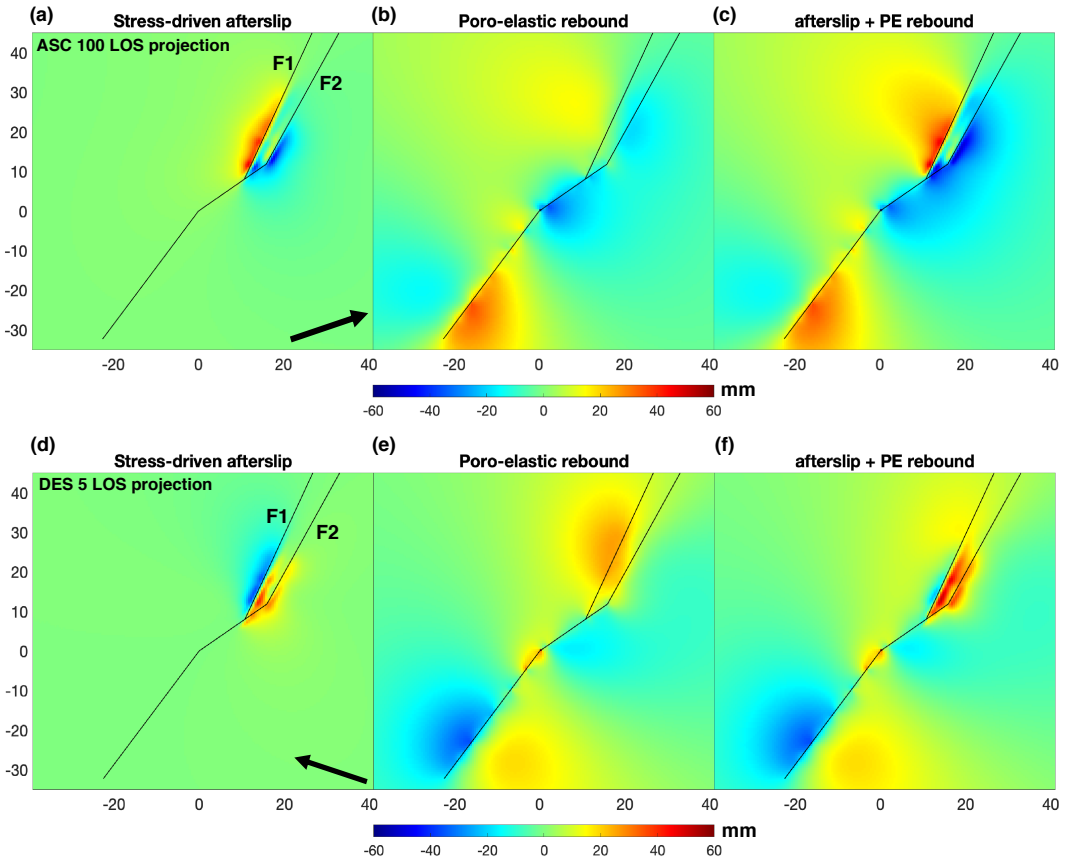

Figure 10. Surface LOS displacements predicted by (a,d) stress-driven afterslip, (b,e) complete poroelastic relaxation and (c,f) a combination of both mechanisms. Other notation is the same as in Figure 8.

0.27, respectively. Figures 10b,e show the predicted surface displacements in the limit of a complete poroelastic relaxation. The poroelastic model predicts positive LOS displacements to the west of the F1 segment for the descending interferograms (Figure 10e), and positive but smaller amplitude LOS displacements for the ascending interferograms (Figure 10b). The assumed values of the drained and undrained Poisson's ratio affect the amplitude, but not the pattern of LOS displacements. Both the pattern and the amplitude of the modeled poroelastic displacements are consistent with InSAR observations (Figures 5 and 7). In particular, poroelastic deformation appears to reduce the misfit between the data and the afterslip models (Figures 8c,f). This suggests that the observed near-field deformation (Figures 5-7) may be indicative of the concurrent occurrence of afterslip and poroelastic rebound (Figures 10c,f). If so, one can estimate in situ hydraulic diffusivity of the upper crust, $\kappa_h = L^2/(\pi t_m)$, where t_m is the time scale of relaxation, and L is the characteristic distance for fluid diffusion. For L on the order of 10 km (representing either the horizontal or the vertical distance for pore fluid flow; note that L scales with the rupture dimensions), and t_m on the order of a few years (Figure 6), κ_h is estimated to be on the order of 1 m^2/s, on a high end of the laboratory and field measurements of hydraulic diffusivities of fractured crystalline rocks (Roeloffs, 1996; Talwani et al., 1999), and comparable to the inferred values from observations of similar-size strike-slip earthquakes (e.g., Fialko, 2004a). Shorter diffusion distances (e.g., in case of pore fluid flow in the shallow crust, or near the fault) would imply smaller values of κ_h.

3.3 Viscoelastic Relaxation

Large earthquakes perturb stresses in the ductile substrate which can respond by producing increased strain rates, and geodetically detectable time-dependent deformation at the Earth's surface (e.g., Elsasser, 1969; Pollitz, 2003; Hetland & Hager, 2005; Takeuchi & Fialko, 2012). The wavelength of such deformation is controlled by the thickness of the elastic layer or the depth of the low-viscosity layer, and the time scale is controlled by the effective viscosity of the ductile medium. To evaluate a possible contribution of viscoelastic relaxation, we performed forward simulations assuming a vertically stratified viscoelastic halfspace. The viscoelastic model is parameterized in terms of the elastic upper crust thickness H, the lower crust viscosity η_1 and the upper-mantle viscosity η_2. In our models, the crust-mantle boundary is fixed at a depth of 65 km, but the thickness of the elastic layer H is allowed to vary between 12 and 50 km. The viscosities of both the lower crust η_1 and the upper mantle η_2 are considered in the range of $10^{16} \sim 10^{20}$ Pa s. The simulations were performed using the code PSGRN-PSCMP (R. Wang et al., 2006).

Figures S15-S17 show the predicted LOS displacements for a range of model parameters H, η_1 and η_2. For $H > 20$ km (Mechie et al., 2012), all viscoelastic models predict four lobes of LOS displacements with amplitude ranging from millimeters to ~ 0.1 m, and wavelength between 10-100 km. The four-lobe pattern is controlled by a vertical component of surface displacements, and its asymmetry is due to a contribution of horizontal displacements projected onto the satellite line of sight. Horizontal displacements dominate the LOS component in case of a relatively thin ($H = 12$ km) elastic layer (Figure S17a). Results shown in Figures S15-S17 can be compared to the observed postseismic LOS displacements over 5 years after the 2015 mainshock (Figure 5). While the InSAR data have a limited spatial coverage due to decorrelation, they provide useful constraints on a range of admissible models. In particular, better correlated and less noisy data from the ascending track (Figure 5a) do not show systematic positive far-field LOS displacements in the NW and SE quadrants of the earthquake rupture which are predicted by viscoelastic models (Figures S15-S17). The latter also predict long-wavelength negative LOS displacements to the east of the earthquake rupture, which are also not observed (Figure 5a). The InSAR data in fact do not show any long-wavelength deformation patterns above the noise level (10-20 mm), which appears to rule out a low-viscosity zone ($\eta_1 < 10^{19}$ Pa s) in the lower crust beneath Pamir (Figure S15). Essentially, the data indicate that the contribution of viscoelastic de-

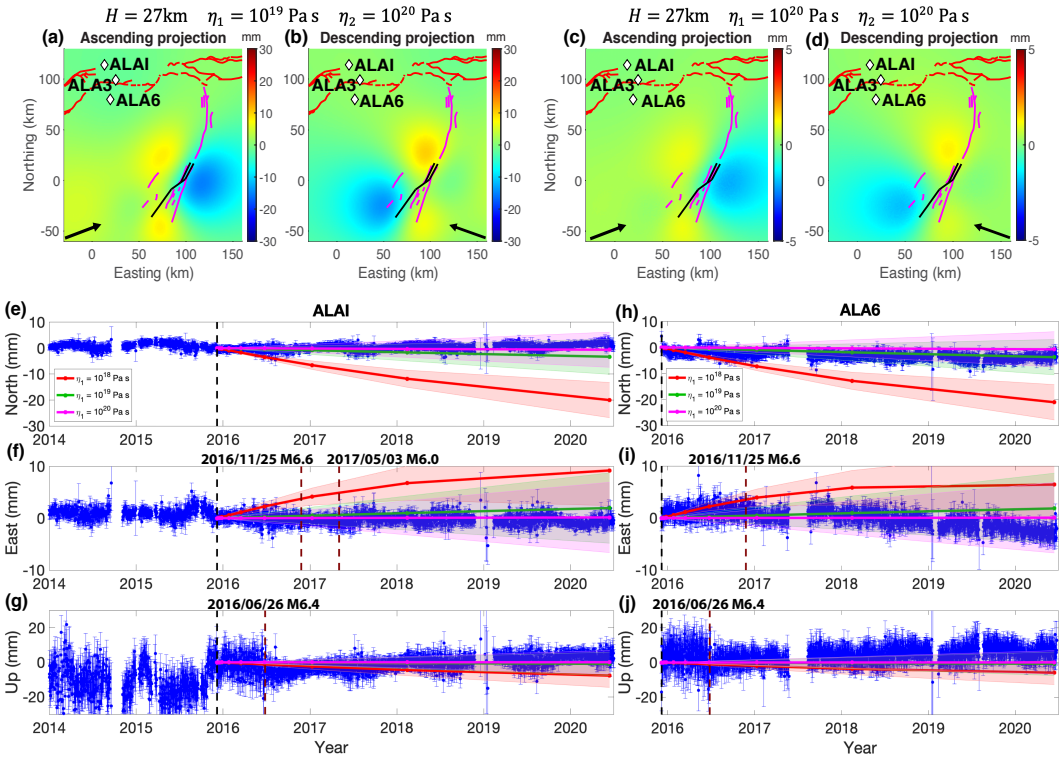

Figure 11. (a-d) Surface LOS displacements predicted by the "best-fit" three-layer viscoelastic model. Model parameters are indicated at the top of the respective panels. (e-j) A comparison between the observed GNSS time-series from continuous sites ALA6 and ALAI, and predictions of viscoelastic models shown in panels a-d, at the respective GNSS site locations. Blue dots and error bars denote daily positions and their uncertainties, respectively. All models assume viscosity of the upper mantle of 10^{20} Pa s. Solid color lines correspond to different assumed viscosities of the lower crust. Color shading represents an admissible range of model predictions due to uncertainties in the estimated pre-seismic velocity of ±1.5 mm/yr (Zubovich et al., 2016). Black vertical dashed line represents the time of the M7.2 Sarez earthquake. Coseismic offsets due to M6+ events (see Table S2) were removed from the GNSS time series.

formation, if any, has to be sufficiently small to be below the detection limit. Figures 11a-d show predictions of a few viscoelastic models that satisfy this constraint.

These inferences are confirmed by the GNSS data from permanent sites ALAI, ALA3, and ALA6 (Figure 11a). Figure 11e-j shows the GNSS time series of displacements for sites ALAI and ALA6, and Figure S18 shows the respective data for site ALA3. In order to identify transient deformation, we removed pre-earthquake velocities from the east and north components of the displacement time series. Pre-earthquake velocities were estimated by the least-squares fitting of a linear function to the displacement timeseries collected before December of 2015. Because site ALA6 was installed several months before the 2015 Sarez earthquake, pre-earthquake data are not enough to estimate pre-seismic velocities. Therefore the east and north components of the displacement time series for site ALA6 were detrended using pre-seismic velocities from the nearby site ALA3 (Figure S18). We also estimated and removed coseismic offsets due to the 2015 Sarez earthquake. The north components of the coseismic offsets showed a good agreement with predictions of the coseismic slip models, while the east components were systematically larger (by a few millimeters) than

the model predictions. The GNSS time series also show coseismic offsets due to several M6+ earthquakes that occurred following the 2015 mainshock (Figure 11e-j). The earthquake-related offsets were estimated using 1 month of data before and after the respective events. The estimated offsets (see Table S2) were removed from the GNSS timeseries. The corrected timeseries are shown in Figures 11e-j. For comparison, we also show predictions of several models assuming various effective viscosities of the lower crust. To account for uncertainties in pre-earthquake velocities, we show a range of model predictions for each assumed value of the lower crustal viscosity (see Figures 11e-j and S18).

Both the GNSS (Figures 11e-j and S18) and InSAR (Figure 5) data put a lower bound on the effective viscosities of both the lower crust and the upper mantle of $\sim 10^{19}$ Pa s (Figure S16). The data also seem to disfavor models assuming a thick elastic layer and a deep low-viscosity channel (Figure S17c). Admissible viscoelastic models (e.g., Figure 11a-d) are characterized by a long-wavelength but small-amplitude signal that is essentially below the noise level of postseismic observations (Figures 5 and 7a). The GNSS data (Figures 11e-j and S18) are most consistent with models assuming the effective viscosity of 10^{19} Pa s or greater for both the lower crust and the upper mantle, i.e., suggesting a negligible contribution from viscoelastic relaxation over the period of observations.

4 Were Large Regional Events Triggered by the 2015 Mainshock?

The 2015 Sarez earthquake was followed by a notable regional seismicity, including a pair of M6+ earthquakes that occurred within one year and ∼100 km to the northeast of the earthquake rupture (see Figure 1). The earlier M6.4 event occurred in June of 2016 within the PTS. The focal mechanism of this event indicates a predominantly thrust faulting (with $\sim 67^\circ$ dip and 266° strike). The later M6.6 earthquake occurred in November of 2016 on the right-lateral Muji fault, and had a dip of $\sim 84^\circ$, and strike of 110°.

A close spatiotemporal correlation between the M7.2 Sarez earthquake and a sequence of M6+ events suggests causal relationships, and raises a question about possible triggering mechanisms. A number of static (e.g., King et al., 1994; Ziv & Rubin, 2000), quasi-static (e.g., Segall, 1989; Jonsson et al., 2003) and dynamic models (e.g., Lomnitz, 1996; Gomberg & Johnson, 2005; Tymofyeyeva et al., 2019) were proposed to explain the triggering mechanisms and stress-mediated interactions between earthquakes. For the Pamir earthquake sequence, large distances (~ 100 km) and temporal intervals (> 0.5 year) between the M7.2 and the subsequent M6+ events imply long-range time-dependent interactions.

To address the question "Were the M6+ events triggered by the M7.2 Sarez earthquake, and if so, what was the triggering mechanism?", we evaluated static Coulomb stress changes due to the mainshock. We used a finite-fault model derived for the M7.2 event (Figure 3) to compute static stress changes at the hypocenters of the two M6+ events that occurred to the north-east of the mainshock (Figure 1). Figure 12 shows the static stress perturbations due to the M7.2 event at the nucleation site of the June 2016 M6.4 event. The latter is assumed to have a NW dipping rupture plane striking 248° and a hypocenter depth of 10 km (He, Hetland, et al., 2018). Figure 13 shows the respective stress perturbations for the November 2016 M6.6 event, using a SE dipping rupture plane striking 110°, as confirmed by relocated aftershocks (J. Chen et al., 2016), at the hypocenter depth of 10 km. We also considered stress changes imposed by the M6.4 event at the hypocenter of the subsequent M6.6 event (Figure S19).

As one can see from Figures 12 and 13, static stress changes caused by the M7.2 event at the locations of the M6+ earthquakes are on the order of kilopascals. Assuming the effective coefficient of friction of 0.4 (King et al., 1994; Tembe et al., 2006; Fialko, 2021), the Coulomb stress changes resolved on the rupture planes of the June 2016 M6.4 and the November 2016 M6.6 earthquakes are -0.3 kPa and 3.4 kPa, respectively. Thus static Coulomb stress changes due to the M7.2 event only mildly encouraged nucleation of the M6.6

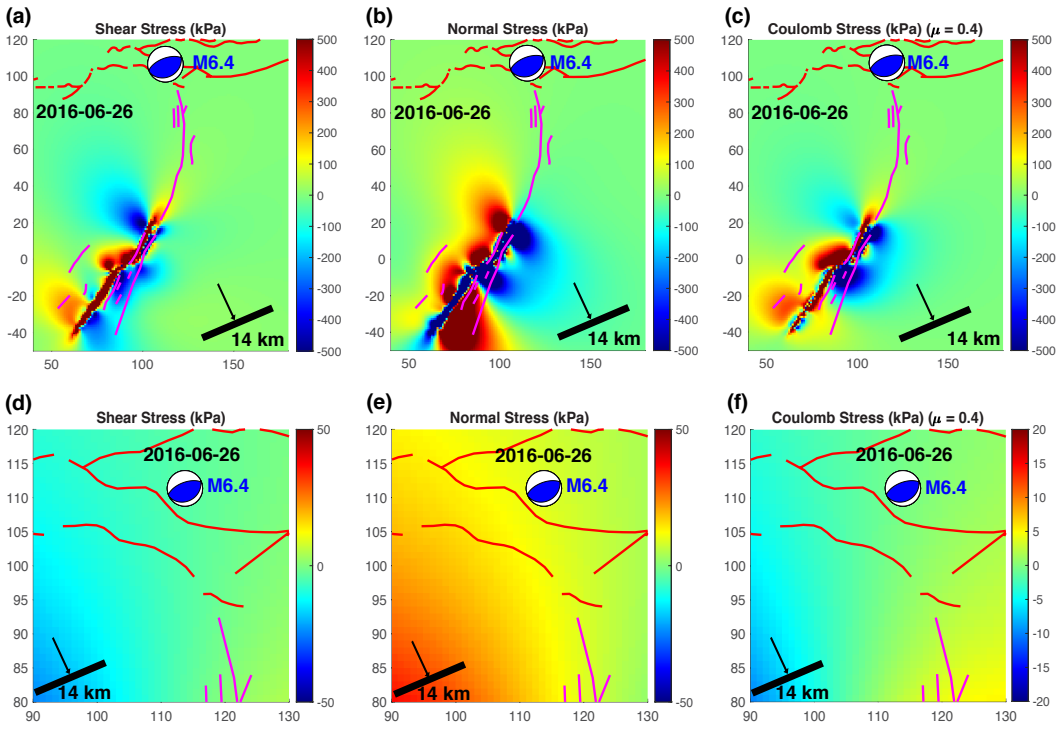

Figure 12. Static stress changes, in kilopascals, due to the M7.2 earthquake at the hypocenter of the June 26, 2016 M6.4 event. Stress changes are computed at the hypocenter depth of 14 km, assuming the average strike of the M6.4 rupture of 248°, and the coefficient of friction of 0.4. (a-c) A regional map. (d-e) A close-up map.

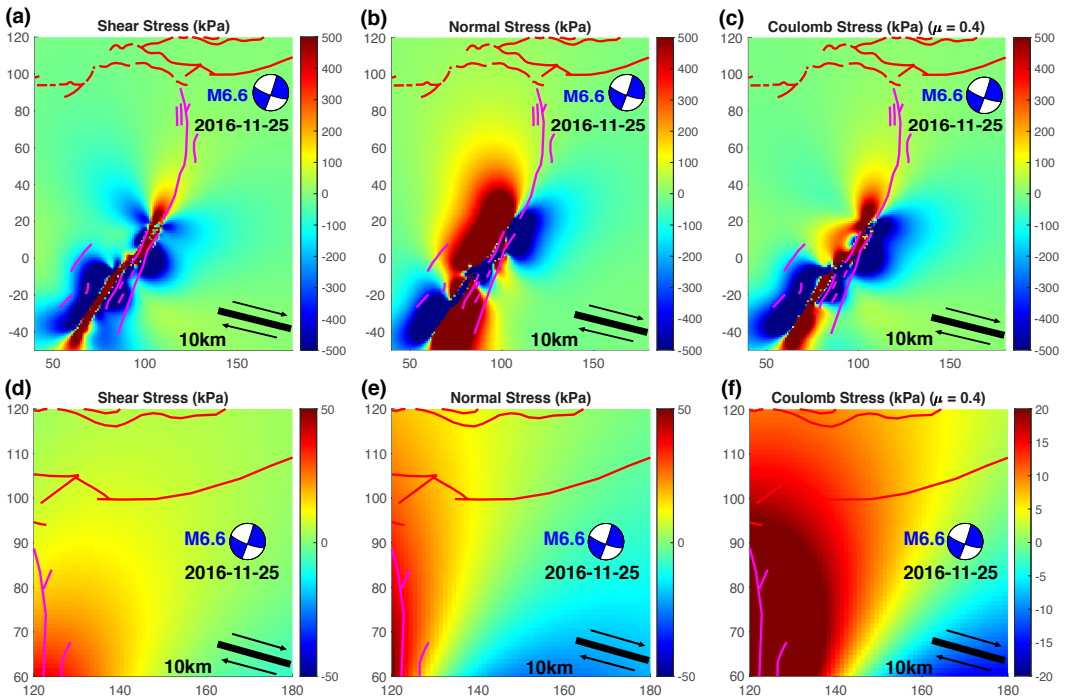

Figure 13. Static stress changes, in kilopascals, due to the M7.2 earthquake at the hypocenter of the November 25, 2016 M6.6 event. Stress changes are computed at depth of 10 km, assuming the average strike of the M6.6 rupture of 107°. Other notation is the same as in Figure 12.

event, and actually discouraged nucleation of the M6.4 event. Results shown in Figure S19 indicate that the M6.6 event was discouraged by the M6.4 event, with a negative resolved Coulomb stress of −1.34 kPa, comparable to, but smaller than the positive stress change caused by the M7.2 mainshock. We also evaluated the time-dependent stress changes due to a possible viscoelastic relaxation following the M7.2 earthquake. Figure S20 shows the Coulomb stress changes predicted by a viscoelastic model constrained by the InSAR and GNSS data (Figures 6 and 11c,d) over a time period of 1 year following the 2015 earthquake. The calculated time-dependent stress changes due to viscoelastic effects are almost zero, as expected given a very limited viscoelastic response. The same is true for stress changes due to poro-elastic relaxation, because of a large distance from the mainshock. Based on these results, we conclude that triggering relationships (if any) between the M7.2 event and a pair of M6+ earthquakes that occurred to the northeast of the mainshock were not based on static or quasi-static stress transfer.

5 Discussion

The Sarez-Karakul fault system accommodates sinistral shear and approximately east-west extension between the relatively quiescent eastern Pamir and the more seismically active western Pamir blocks (Figure 1). The epicenter of the 2015 M7.2 Sarez earthquake is located sufficiently close to the epicenter of the 1911 M7.3 event (Kulikova et al., 2016) to raise a possibility that the two earthquakes ruptured the same fault. Based on the analysis of synthetic seismograms, Elliott et al. (2020) proposed that the 1911 earthquake may have indeed nucleated at the southern end of the SKFS. Assuming a secular rate of shear motion between the eastern and western Pamir of 5 ± 2 mm/yr (Metzger et al., 2017), the time interval between the last and the penultimate event of $\sim 10^2$ yrs is one to two orders of magnitude smaller than the estimated average recurrence interval (average coseismic slip divided by the secular slip rate) of $10^3 - 10^4$ yrs. The 1911-2015 sequence may thus be an example of re-rupturing of the same fault system within a relatively short period of time.

Given that the 2015 earthquake occurred on an unmapped (or a partially mapped) fault having a complex geometry with variable strike and dip (Figure 3) located within a distributed deformation zone at the southern end of the Sarez-Karakul fault system (Figures 1 and 2), the respective fault is likely in a developing stage. Manighetti et al. (2007) suggested that the degree of fault maturity can be inferred from the along-strike slip distribution and the static stress drop. According to their classification, young and developing faults are characterized by (i) higher stress drops and (ii) along-strike slip distributions that are symmetric with respect to the middle of the earthquake rupture (Manighetti et al., 2007). Based on such criteria, the fault that produced the 2015 event can be classified as mature based on the maximum slip to rupture length ratio, and as immature based on the largely symmetric slip distribution along the earthquake rupture (Figures 3 and 4). Other indicators of fault maturity may include e.g. details of slip distribution with depth (Dolan & Haravitch, 2014), as discussed below.

The 2015 event shares a number of similarities with other major shallow earthquakes that occurred on relatively immature strike-slip faults. One common emergent feature is slip partitioning between the closely spaced sub-parallel fault branches, such as those identified at the NE end of the 2015 rupture based on coseismic SAR offsets (Figures S1 and S5), postseismic LOS displacements (Figure 7), and geologically mapped fault traces (Figure S5; Elliott et al., 2020). Similar rupture patterns were also observed in recent M7+ events (Fialko et al., 2001; Simons et al., 2002; Jin & Fialko, 2020, 2021). Coseismic slip on sub-parallel fault strands is puzzling because slip on a given fault interface decreases shear stress, and therefore discourages slip on nearby similarly oriented interfaces (e.g., Harris & Day, 1993; King et al., 1994; Yamashita & Umeda, 1994). Field observations and numerical models indicate that earthquake ruptures can jump from one fault to another across step-overs and other discontinuities, provided that the distance between sup-parallel fault branches is less than ~ 5 km (e.g., Harris & Day, 1993; Kase & Kuge, 2001). Dynamic ruptures may

also have a tendency to bifurcate due to highly perturbed stresses around the propagating rupture fronts (e.g., Kame & Yamashita, 1999; Poliakov et al., 2002). Large off-fault stress perturbations associated with dynamic rupture fronts may contribute to secondary faulting within wide damage zones (Wallace & Morris, 1986; Fialko et al., 2002). In case of the 2015 Sarez earthquake, Sangha et al. (2017) observed a sudden increase in the rupture speed and high frequency radiation at the NE kink of the fault trace that corresponds to a bifurcation point in our model (Figure 2). However, particular mechanisms that enable slip on multiple sub-parallel fault strands remain unclear. A comparison of coseismic slip distribution on the activated fault branches at the NE end of the earthquake rupture (F1 and F2, Figure 7) shows a complementary pattern of slip amplitudes, such that areas of high slip on one fault are associated with reduced slip on the neighboring fault (Figure S21). As one can see in Figure S19, much of the coseismic slip on the F1 segment occurred in the depth range of $5-10$ km, whereas slip on the F2 segment occurred predominantly in the depth range of $1-4$ km. Inversions of surface displacement data for slip distribution on closely spaced faults suffer from a limited resolution at depth comparable to the spacing between the faults. In order to test the model sensitivity to alternative fault geometries, we performed an additional set of simulations in which we allowed segments F1 and F2 to merge at depth. Results are shown in Figure S22. Because of a change in the dip angle of the eastern branch (from the west-dipping to the east-dipping) required in case of a "Y-shaped" intersection (see Figure S22d), the fit to the coseismic displacement data is degraded on the west side of segment F1 (see Figure S22c). Therefore we conclude that the two fault branches unlikely merge in the upper half of the seismogenic layer. The anti-correlated pattern of slip on sub-parallel fault strands suggested by our kinematic inversions is easier to reconcile with predictions of dynamic rupture models (e.g., Kase & Kuge, 2001), and may provide an explanation for multi-stranded coseismic ruptures observed elsewhere (e.g., Fialko et al., 2001; Simons et al., 2002; Jin & Fialko, 2020, 2021).

The seismic moment release as a function of depth for the 2015 event is also similar to the seismic moment release for other M7 earthquakes that occurred on relatively immature faults. Figure 14 shows the coseismic slip averaged along strike vs depth for the 2015 Sarez earthquake (black line) as well as several other M7 earthquakes (color lines). The maximum along-strike averaged slip due to the M7.2 Sarez earthquake occurred in the depth interval of 3-5 km, essentially the same as for similar-sized strike-slip earthquakes analyzed using a consistent methodology (Fialko et al., 2005; Y. Wang et al., 2014; Jin & Fialko, 2020, 2021). The estimated slip glut with respect to surface offsets is on the order of $\sim 20-30\%$. Such a behavior can be attributed to: (i) velocity-strengthening friction in the top few kilometers of the Earth's crust that inhibits coseismic slip (e.g., Goulty & Gilman, 1978; Bilham & Behr, 1992; Scholz, 1998; Barbot, Fialko, & Bock, 2009; Lindsey & Fialko, 2016; Jin & Fialko, 2021); (ii) the effect of reduced elastic moduli in a wide damage zone around the earthquake rupture (e.g., Rybicki & Kasahara, 1977; Barbot, Fialko, & Sandwell, 2008, 2009), and (iii) off-fault yielding due to dynamic stress perturbations (e.g., Kaneko & Fialko, 2011; Roten et al., 2017). Coseismic variations in slip in the top 3-5 km of the upper crust that are not balanced by the postseismic and interseismic creep are referred to as shallow slip deficit (SSD) (Fialko et al., 2005). Field observations suggest that the magnitude of the SSD may inversely correlate with structural maturity of fault zones (e.g., Dolan & Haravitch, 2014; Zinke et al., 2014).

Our results suggest that some shallow afterslip occurred at the NE end of the earthquake rupture (Figures 5 and 7). While the coverage is limited due to decorrelation, available data suggest that shallow afterslip did not occur along the entire rupture trace (Figure 7a). This, along with the estimated amount of shallow afterslip (maximum amplitude of 0.2-0.3 m over 5 years, Figures 9 and S14) indicates that the afterslip alone cannot account for the average coseismic slip deficit on the order of 1 m (Figures 3 and 14). The remaining deficit might possibly be attributed to interseismic creep, effects of a compliant fault zone, coseismic off-fault damage, or some combination of the above. Development of a soft damage zone around the SKFS may be enhanced due to the Quaternary deposits in the Kokuibel Valley (Elliott

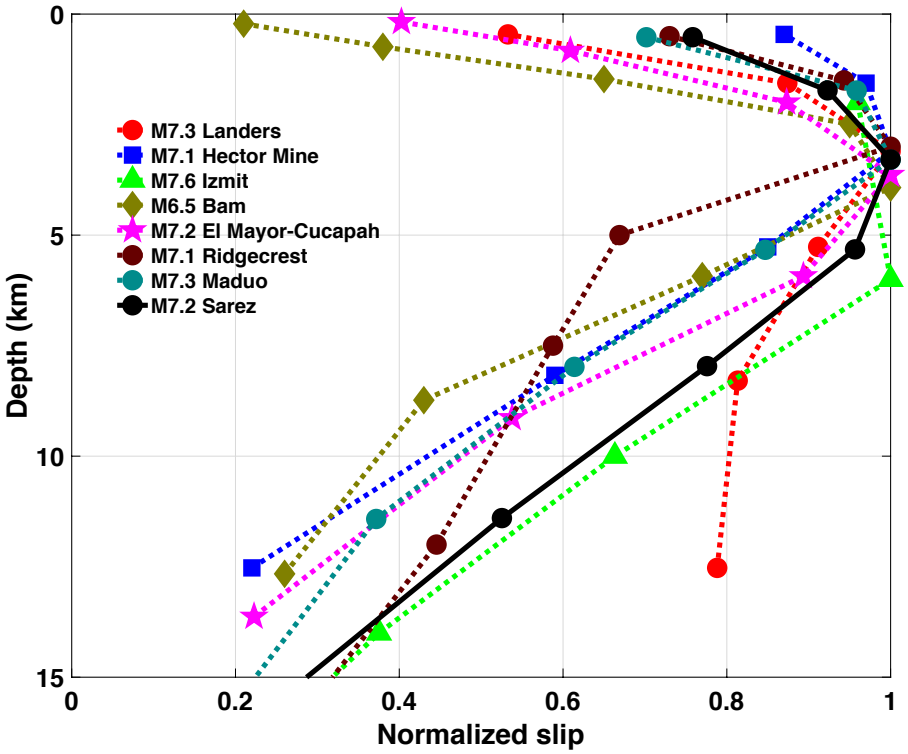

Figure 14. Along-strike averaged coseismic slip as a function of depth for the M 7.2 Sarez (Pamir) earthquake (black solid line), as well as for several other M∼ 7 strike-slip earthquakes (color dashed lines, data from Fialko et al. (2005); Kaneko and Fialko (2011); Jin and Fialko (2020, 2021)).

et al., 2020). The Quaternary deposits are gravels related to alluvial fans and glaciofluvial terraces, which are drained by the sediments along the Kokuibel River (Strecker et al., 1995). The same deposits may be responsible for the velocity-strengthening behavior in the top few kilometers, as evidenced by the occurrence of shallow afterslip. Our models show that the most robust afterslip occurs on the F1 fault segment (Figure 9a) located in the middle of the Kokuibel valley, where the alluvial deposits are presumably the thickest.

It is worth noting that shallow afterslip imaged by InSAR observations is not localized to a fault trace, but instead is distributed over a shear zone that is a few kilometers wide (Figure 7b). Similar shear zones have been suggested by observations of interseismic deformation on the Southern San Andreas (Lindsey, Fialko, et al., 2014) and San Jacinto (Lindsey, Sahakian, et al., 2014) faults, and postseismic creep on the North Anatolian (Cakir et al., 2012) and the Kunlun Pass and Xidatan (D. Zhao et al., 2021) faults. In case of the Southern San Andreas fault, the degree of strain localization due to shallow interseismic creep appears to be controlled by the local stress regime, such that localized creep occurs on transpressional fault segments, and distributed creep occurs on transtensional fault segments (Lindsey, Fialko, et al., 2014). These insights may be relevant to observations of a broad shear zone that accommodates afterslip following the 2015 Sarez earthquake (Figure 7), given a transtensional nature of the SKFS (Strecker et al., 1995; Schurr et al., 2014). A distributed creep may also result from inelastic deformation within poorly consolidated surface materials deposited in the Kokuibel Valley (Elliott et al., 2020). The same feature may also be responsible for the "buried" shallow afterslip in kinematic inversions (Figure S14) which assume that fault slip is perfectly localized.

The timeseries of LOS displacements across the fault trace in the NE part of the earthquake rupture (Figures 5 and 6) reveal a multi-year deformation transient with a gradually decaying rate until early 2019, when a secondary deformation episode is suggested by the data. We have checked the earthquake catalogs and did not find any events with magnitude greater than 4 within 100 km from the epicenter of the 2015 Sarez earthquake. While the long-range triggering of fault creep by the dynamic stress changes from seismic waves has been observed (e.g., Tymofyeyeva et al., 2019), we note that such triggering is expected when the target fault is on a verge of nucleating a spontaneous slow slip event (Tymofyeyeva et al., 2019), which is less likely during a robust afterslip sequence. We also point out that a similar pattern of LOS displacements from different look directions (see Figure 6b) cannot be explained by a pure strike-slip motion (see Figure 10a,d), but could possibly result from some contribution of dip-slip (west side up), and/or poro-elastic effects (Figure 10b,e). Particular mechanisms responsible for non-monotonic rates of postseismic deformation, however, remain unclear.

On a larger scale, the available InSAR data (Figures 5 and S13) do not reveal spatially coherent lobes of LOS displacements expected in case of robust viscoelastic relaxation (Figures 11 and S15-S17). This contrasts with observations of postseismic deformation due to similar-size strike-slip earthquakes in the Mojave Desert (California, USA), in particular the M7.3 Landers and M7.1 Hector Mine earthquakes, both of which have generated characteristic patterns of LOS displacements having amplitude of several centimeters and wavelength of a few tens of kilometers over a time period of several years following the mainshock (Fialko, 2004a; Takeuchi & Fialko, 2013). The lack of a detectable signature of viscoelastic relaxation due to the Sarez earthquake is confirmed by the data from the continuously recording GNSS sites located within $\sim$ 100 km from the ruptured fault (Figures 11). Based on results of forward models exploring a wide parameter space (Figures 11 and S15-S17), we conclude that deformation in the near-to-intermediate field (within 1-2 rupture lengths from the earthquake rupture) does not reveal a clear contribution of visco-elastic relaxation in the lower crust or upper mantle. While our forward models assume a simple linear Maxwell rheology, the predicted patterns of surface displacements are not strongly dependent on a particular type of the assumed constitutive law. For a given duration of

observations, different assumed rheologies mostly affect the predicted amplitude of surface displacements.

Results presented above are in line with several previous studies that used multi-year observations of postseismic response due to earthquakes that occurred at the margins of the Tibetan Plateau and the adjacent regions (Barbot, Hamiel, & Fialko, 2008; K. Wang & Fialko, 2014, 2018). These results lend support to models assuming a relatively strong lithosphere with crustal blocks bounded by deeply rooted faults that accommodate most of the internal deformation (e.g., Avouac & Tapponnier, 1993; Hubbard & Shaw, 2009). Alternative models envision a persistent low-viscosity channel underlying high-elevation areas (e.g., W.-L. Zhao & Morgan, 1987; Royden et al., 1997; Shapiro et al., 2004). In particular, Clark and Royden (2000) suggested that the low topographic gradient margins such as that between Pamir and the Tarim basin (Figure 1) can be interpreted in terms of viscous pressure losses in a lower crustal channel having viscosity as low as $10^{16} - 10^{17}$ Pa s beneath the high elevation areas. Our results (Figure 11) place a lower bound on the effective viscosity in the lower crust beneath the Central Pamir of 10^{19} Pa s (i.e., implying a negligible viscoelastic response on a time scale of observations). The same conclusions were reached for the lithosphere underlying the epicentral regions of the 2005 M7.6 Kashmir (K. Wang & Fialko, 2014) and the 2015 M7.8 Gorkha (K. Wang & Fialko, 2018) earthquakes. Regions with lower transient viscosity on the order of $10^{18} - 10^{19}$ Pa s may exist further in the Tibet interior as evidenced by e.g. far-field postseismic deformation detected by GNSS observations (e.g., Huang et al., 2014; B. Zhao et al., 2017; D. Zhao et al., 2021).

A pair of strong (M6+) earthquakes that occurred within one year of the M7.2 Sarez earthquake on the nearby fault systems (Figure 1) appears to have a significant spatio-temporal correlation with the 2015 mainshock. In particular, as many M6+ events occurred in the study area over 50 years prior to the 2015 earthquake as over 1 year following the earthquake; in addition, regional seismicity exhibits strong clustering (Figure S23). Because of a large ($\sim 10^2$ km) distance between the 2015 rupture and the subsequent M6+ earthquakes, the amplitude of static stress changes is small. However, given that a threshold for triggering by static stress changes may be very low (e.g., Ziv & Rubin, 2000), it is of interest to establish if the static stress changes encouraged or discouraged nucleation of distant "aftershocks". Results presented in Section "Were Large Regional Events Triggered by the 2015 Mainshock?" provide quantitative constraints on the magnitude of static stress changes, and furthermore demonstrate that in some cases the static stress changes actually brought the respective faults further away from failure. This, along with the vanishingly small amplitudes of static stress perturbations (Figures 12 and 13) argues that the latter are not responsible for triggering of the M6+ events. The same applies to quasi-static stress changes (e.g., due to viscoelastic relaxation, Figure S20). It follows that causal relations (if any) between the M7.2 Sarez earthquake and the subsequent M6+ events may have involved delayed dynamic triggering (e.g., Parsons, 2005; Hill, 2008; Shelly et al., 2011). We note that the location of the potentially triggered M6+ events is aligned with the radiation pattern of the 2015 mainshock which nucleated at the south end of the earthquake rupture and propagated to the north-east (Figures 1 and S23). For both M6+ events, eventual nucleation proceeded despite negative static stress changes induced by previous events. This is similar to the stressing history at the nucleation site of the 2019 M7.1 Ridgecrest earthquake in Eastern California constrained by dislocation models based on seismic and geodetic data (Jin & Fialko, 2020; Fialko & Jin, 2021).

6 Conclusions

The 2015 M_w7.2 Sarez earthquake occurred in the Pamir orogen at the NW margin of the Tibetan Plateau. We presented space geodetic (InSAR and GNSS) observations and models of coseismic and postseismic deformation due to the Sarez earthquake. The earthquake ruptured a NNE trending left-lateral fault of the Sarez-Karakul fault system. Geodetic data reveal a ∼70-80 km-long rupture with the maximum offset of ∼3-4 meters on

the SW and central fault segments, and two sub-parallel fault strands with smaller offsets at the NE end of the rupture. Time series of postseismic displacements spanning ∼5 years after the mainshock reveal afterslip at the NE end of the rupture with a total amplitude of a few hundreds of millimeters, occurring primarily at the periphery of seismic asperities. The observed afterslip compensates a fraction of the coseismic shallow slip deficit (SSD). Analysis of postseismic InSAR data from different lines of sight is suggestive of an additional contribution of poroelastic relaxation in the upper crust. The absence of systematic LOS displacement patterns on spatial scales on the order of the rupture length and above, as well as the absence of transient signals in the GNSS time series provide constraints on the effective rheological properties of the lower crust and upper mantle beneath Pamir. Our simulations suggest a lower bound on the effective viscosity of the ductile substrate of 10^{19} Pa s (i.e., a negligible contribution from viscoelastic relaxation). These findings point out to a relatively strong lower crust in the NW corner of the Tibetan Plateau. We also analyzed possible triggering relationships between the M7.2 event and a pair of strong (M6+) earthquakes that occurred within one year and ∼ 100 km NNE from the mainshock. The amplitude and sign of the calculated stress perturbations due to the M7.2 event on the rupture planes of M6+ events rule out triggering by static or quasi-static stress transfer. If the M6+ events were indeed advanced by the M7.2 mainshock, one possible mechanism is delayed dynamic triggering.

Data Availability Statement

The original InSAR data are available from Alaska Satellite Facility (`https://asf.alaska.edu/data-sets/derived-data-sets/insar/`) and Western North America InSAR (`https://winsar.unavco.org/insar/`). Geologically mapped fault data are available from `https://esdynamics.geo.uni-tuebingen.de/faults/`.

Acknowledgments
We thank Editor Isabelle Manighetti, Associate Editor, Austin Elliott and one anonymous reviewers for comments and suggestions that improved this manuscript. This study was supported by NSF (grant EAR-1841273) and NASA (grant 80NSSC18K0466). Sentinel-1 data were provided by the European Space Agency (ESA) through Alaska Satellite Facility (ASF) and UNAVCO. ALOS-2 data were provided by the Japanese Space Agency (JAXA). The post-processed data archiving at Zenodo is underway. Figures were produced using Generic Mapping Tools (GMT) (Wessel et al., 2013) and Matlab. The authors declare no competing interests.

References

Ahmed, R., Siqueira, P., Hensley, S., Chapman, B., & Bergen, K. (2011). A survey of temporal decorrelation from spaceborne L-Band repeat-pass InSAR. *Remote Sensing of Environment*, *115*(11), 2887–2896.

Avouac, J.-P., & Tapponnier, P. (1993). Kinematic model of active deformation in central Asia. *Geophys. Res. Lett.*, *20*, 895–898.

Barbot, S., & Fialko, Y. (2010a). Fourier-domain Green's function for an elastic semi-infinite solid under gravity, with applications to earthquake and volcano deformation. *Geophys. J. Int.*, *182*, 568–582.

Barbot, S., & Fialko, Y. (2010b). A unified continuum representation of post-seismic relaxation mechanisms: semi-analytic models of afterslip, poroelastic rebound and viscoelastic flow. *Geophys. J. Int.*, *182*, 1124-1140.

Barbot, S., Fialko, Y., & Bock, Y. (2009). Postseismic deformation due to the Mw 6.0 2004 Parkfield earthquake: Stress-driven creep on a fault with spatially variable rate-and-state friction parameters. *J. Geophys. Res.*, *114*, B07405.

Barbot, S., Fialko, Y., & Sandwell, D. (2008). Effect of a compliant fault zone

on the inferred earthquake slip distribution. *J. Geophys. Res.*, *113*, B06404, doi:10.1029/2007JB005256.

Barbot, S., Fialko, Y., & Sandwell, D. (2009). Three-dimensional models of elasto-static deformation in heterogeneous media, with applications to the Eastern California Shear Zone. *Geophys. J. Int.*, *179*, 500–520.

Barbot, S., Hamiel, Y., & Fialko, Y. (2008). Space geodetic investigation of the co- and post-seismic deformation due to the 2003 M_w 7.1 Altai earthquake: Implications for the local lithospheric rheology. *J. Geophys. Res.*, *113*, B03403.

Bechor, N., & Zebker, H. (2006). Measuring two-dimensional movements using a single InSAR pair. *Geophys. Res. Lett.*, *33*, doi:10.1029/2006GL026883.

Bilham, R., & Behr, J. (1992). A two-layer model for aseismic slip on the Superstition Hills fault, California. *Bull. Seism. Soc. Am.*, *82*(3), 1223–1235.

Bullock, R. J., De Paola, N., Holdsworth, R. E., & Trabucho-Alexandre, J. (2014). Lithological controls on the deformation mechanisms operating within carbonate-hosted faults during the seismic cycle. *Journal of Structural Geology*, *58*, 22–42.

Cakir, Z., Ergintav, S., Ozener, H., Dogan, U., Akoglu, A. M., Meghraoui, M., & Reilinger, R. (2012). Onset of aseismic creep on major strike-slip faults. *Geology*, *40*, 1115–1118. doi: 10.1130/G33522.1

Chen, C., & Zebker, H. (2002). Phase unwrapping for large sar interferograms: Statistical segmentation and generalized network models. *IEEE Transactions on Geoscience and Remote Sensing*, *40*, 1709–1719.

Chen, J., Li, T., Sun, J., Fang, L., Yao, Y., Li, Y., ... Fu, B. (2016). Coseismic surface ruptures and seismogenic Muji fault of the 25 November 2016 Aerketao Mw 6.6 earthquake in northern Pamir. *Seismology and Geology*, *38*(4), 1160–1174.

Clark, M. K., & Royden, L. H. (2000). Topographic ooze: Building the eastern margin of Tibet by lower crustal flow. *Geology*, *28*(8), 703–706.

Dieterich, J. (2015). Applications of Rate- and State-Dependent Friction to Models of Fault Slip and Earthquake Occurrence. In G. Schubert (Ed.), *Treatise on geophysics, 2nd. ed., vol. 4* (pp. 93–110). Elsevier Ltd., Oxford.

Dieterich, J. H. (1979). Modeling of rock friction .1. Experimental results and constitutive equations. *J. Geophys. Res.*, *84*(NB5), 2161–2168. doi: 10.1029/JB084iB05p02161

Dolan, J. F., & Haravitch, B. D. (2014). How well do surface slip measurements track slip at depth in large strike-slip earthquakes? The importance of fault structural maturity in controlling on-fault slip versus off-fault surface deformation. *Earth and Planetary Science Letters*, *388*, 38–47.

Elliott, A., Elliott, J., Hollingsworth, J., Kulikova, G., Parsons, B., & Walker, R. (2020). Satellite imaging of the 2015 M 7.2 earthquake in the Central Pamir, Tajikistan, elucidates a sequence of shallow strike-slip ruptures of the Sarez-Karakul fault. *Geophys. J. Int.*, *221*, 1696–1718.

Elsasser, W. M. (1969). Convection and stress propagation in the upper mantle. In S. K. Runcorn (Ed.), *The application of modern physics to the earth and planetary interiors* (pp. 223–249). New York: Wiley.

Farr, T. G., Rosen, P. A., Caro, E., Crippen, R., Duren, R., Hensley, S., ... others (2007). The shuttle radar topography mission. *Reviews of geophysics*, *45*(2).

Fattahi, H., Simons, M., & Agram, P. (2017). InSAR time-series estimation of the ionospheric phase delay: An extension of the split range-spectrum technique. *IEEE Transactions on Geoscience and Remote Sensing*, *55*(10), 5984–5996.

Fialko, Y. (2004a). Evidence of fluid-filled upper crust from observations of post-seismic deformation due to the 1992 M_w7.3 Landers earthquake. *J. Geophys. Res.*, *109*, B08401, 10.1029/2004JB002985.

Fialko, Y. (2004b). Probing the mechanical properties of seismically active crust with space geodesy: Study of the co-seismic deformation due to the 1992 M_w7.3 Landers (southern California) earthquake. *J. Geophys. Res.*, *109*, B03307, 10.1029/2003JB002756.

Fialko, Y. (2015). Fracture and Frictional Mechanics - Theory. In G. Schubert (Ed.), *Treatise on geophysics, 2nd. ed., vol. 4* (p. 73-91). Elsevier Ltd., Oxford.

Fialko, Y. (2021). Estimation of absolute stress in the hypocentral region of the 2019 Ridgecrest, California, earthquakes. *J. Geophys. Res.*, *126*, e2021JB022000.

Fialko, Y., & Jin, Z. (2021). Simple shear origin of the cross-faults ruptured in the 2019 Ridgecrest earthquake sequence. *Nature Geoscience*, *14*, 513–518.

Fialko, Y., Sandwell, D., Agnew, D., Simons, M., Shearer, P., & Minster, B. (2002). Deformation on nearby faults induced by the 1999 Hector Mine earthquake. *Science*, *297*, 1858–1862.

Fialko, Y., Sandwell, D., Simons, M., & Rosen, P. (2005). Three-dimensional deformation caused by the Bam, Iran, earthquake and the origin of shallow slip deficit. *Nature*, *435*, 295–299.

Fialko, Y., Simons, M., & Agnew, D. (2001). The complete (3-D) surface displacement field in the epicentral area of the 1999 M_w7.1 Hector Mine earthquake, southern California, from space geodetic observations. *Geophys. Res. Lett.*, *28*, 3063–3066.

Goldstein, R. M., & Werner, C. L. (1998). Radar interferogram filtering for geophysical applications. *Geophys. Res. Lett.*, *25*, 4035-4038. doi: 10.1029/1998GL900033

Golub, G. H., Hansen, P. C., & O'Leary, D. P. (1999). Tikhonov regularization and total least squares. *SIAM journal on matrix analysis and applications*, *21*(1), 185–194.

Gomba, G., Parizzi, A., De Zan, F., Eineder, M., & Bamler, R. (2015). Toward operational compensation of ionospheric effects in SAR interferograms: The split-spectrum method. *IEEE Transactions on Geoscience and Remote Sensing*, *54*(3), 1446–1461.

Gomberg, J., & Johnson, P. (2005). Dynamic triggering of earthquakes. *Nature*, *437*(7060), 830–830.

Goulty, N. R., & Gilman, R. (1978). Repeated creep events on the San Andreas Fault near Parkfield, California, Recorded by a strainmeter array. *J. Geophys. Res.*, *83*(B11), 5415-5419. doi: 10.1029/JB083iB11p05415

Harris, R. A., & Day, S. M. (1993). Dynamics of fault interaction: Parallel strike-slip faults. *Journal of Geophysical Research: Solid Earth*, *98*(B3), 4461–4472.

He, P., Ding, K., & Xu, C. (2018). The 2016 Mw 6.7 Aketao earthquake in Muji range, northern Pamir: rupture on a strike-slip fault constrained by Sentinel-1 radar interferometry and GPS. *International journal of applied earth observation and geoinformation*, *73*, 99–106.

He, P., Hetland, E. A., Niemi, N. A., Wang, Q., Wen, Y., & Ding, K. (2018). The 2016 Mw 6.5 Nura earthquake in the Trans Alai range, northern Pamir: possible rupture on a back-thrust fault constrained by Sentinel-1A radar interferometry. *Tectonophysics*, *749*, 62–71.

Herring, T. A., Melbourne, T. I., Murray, M. H., Floyd, M. A., Szeliga, W. M., King, R. W., ... Wang, L. (2016). Plate Boundary Observatory and related networks: GPS data analysis methods and geodetic products. *Reviews of Geophysics*, *54*(4), 759–808.

Hetland, E., & Hager, B. (2005). Postseismic and interseismic displacements near a strike-slip fault: A two-dimensional theory for general linear viscoelastic rheologies. *Journal of Geophysical Research: Solid Earth*, *110*(B10).

Hill, D. P. (2008). Dynamic stresses, Coulomb failure, and remote triggering. *Bull. Seism. Soc. Am.*, *98*, 66–92.

Hooper, A., & Zebker, H. (2007). Phase unwrapping in three dimensions with application to InSAR time series. *J. Optical Soc. of America.*, *24*, 2737–2747.

Huang, M.-H., Bürgmann, R., & Freed, A. M. (2014). Probing the lithospheric rheology across the eastern margin of the Tibetan Plateau. *Earth Planet. Sci. Lett.*, *396*, 88–96.

Hubbard, J., & Shaw, J. H. (2009). Uplift of the Longmen Shan and Tibetan plateau, and the 2008 Wenchuan (M= 7.9) earthquake. *Nature*, *458*(7235), 194.

Ischuk, A., Bendick, R., Rybin, A., Molnar, P., Khan, S. F., Kuzikov, S., ... others (2013). Kinematics of the Pamir and Hindu Kush regions from GPS geodesy. *J. Geophys. Res.*, *118*, 2408–2416.

Jin, Z., & Fialko, Y. (2020). Finite slip models of the 2019 Ridgecrest earthquake sequence constrained by space geodetic data and aftershock locations. *Bull. Seism. Soc. Am.*, *110*, 1660–1679.

Jin, Z., & Fialko, Y. (2021). Coseismic and early postseismic deformation due to the 2021 M7.4 Maduo (China) earthquake. *Geophys. Res. Lett.*. doi: 10.1029/2021GL095213

Jonsson, S., Segall, P., Pedersen, R., & Bjornsson, G. (2003). Post-earthquake ground movements correlated to pore-pressure transients. *Nature*, *424*, 179–183.

Kame, N., & Yamashita, T. (1999). Simulation of the spontaneous growth of a dynamic crack without constraints on the crack tip path. *Geophys. J. Int.*, *139*, 345–358.

Kaneko, Y., & Fialko, Y. (2011). Shallow slip deficit due to large strike-slip earthquakes in dynamic rupture simulations with elasto-plastic off-fault response. *Geophys. J. Int.*, *186*, 1389–1403.

Kase, Y., & Kuge, K. (2001). Rupture propagation beyond fault discontinuities: significance of fault strike and location. *Geophysical Journal International*, *147*(2), 330–342.

King, G. C. P., Stein, R. S., & Lin, J. (1994). Static stress changes and the triggering of earthquakes. *Bull. Seismol. Soc. Am.*, *84*, 935–953.

Kufner, S.-K., Schurr, B., Haberland, C., Zhang, Y., Saul, J., Ischuk, A., & Oimahmadov, I. (2017). Zooming into the Hindu Kush slab break-off: A rare glimpse on the terminal stage of subduction. *Earth and Planetary Science Letters*, *461*, 127–140.

Kulikova, G., Schurr, B., Krüger, F., Brzoska, E., & Heimann, S. (2016). Source parameters of the Sarez-Pamir earthquake of 1911 February 18. *Geophysical Journal International*, *205*(2), 1086–1098.

LaBonte, A., Brown, K., & Fialko, Y. (2009). Hydrogeologic detection and finite-element modeling of a slow-slip event in the Costa Rica prism toe. *J. Geophys. Res.*, *114*, B00A02, doi:10.1029/2008JB005806.

Lapusta, N., Rice, J. R., Ben-Zion, Y., & Zheng, G. (2000). Elastodynamic analysis for slow tectonic loading with spontaneous rupture episodes on faults with rate- and state-dependent friction. *J. Geophys. Res.*, *105*(B10), 23765–23789.

Lindsey, E. O., & Fialko, Y. (2016). Geodetic constraints on frictional properties and earthquake hazard in the Imperial Valley, Southern California. *J. Geophys. Res.*, *121*(2), 1097–1113. (2015JB012516) doi: 10.1002/2015JB012516

Lindsey, E. O., Fialko, Y., Bock, Y., Sandwell, D. T., & Bilham, R. (2014). Localized and distributed creep along the southern San Andreas Fault. *J. Geophys. Res.*, *119*(10), 7909–7922.

Lindsey, E. O., Sahakian, V. J., Fialko, Y., Bock, Y., Barbot, S., & Rockwell, T. K. (2014). Interseismic strain localization in the San Jacinto fault zone. *Pure Appl. Geophys.*, *171*(11), 2937–2954.

Lohman, R. B., & Simons, M. (2005). Some thoughts on the use of InSAR data to constrain models of surface deformation: Noise structure and data downsampling. *Geochemistry, Geophysics, Geosystems*, *6*(1).

Lomnitz, C. (1996). Search of a worldwide catalog for earthquakes triggered at intermediate distances. *Bull. Seism. Soc. Am.*, *86*, 293–298.

Manighetti, I., Campillo, M., Bouley, S., & Cotton, F. (2007). Earthquake scaling, fault segmentation, and structural maturity. *Earth Planet. Sci. Lett.*, *253*, 429–438.

Marone, C. (1998). Laboratory-derived friction laws and their application to seismic faulting. *Annu. Rev. Earth Planet. Sci.*, *26*, 643–696.

Mechie, J., Yuan, X., Schurr, B., Schneider, F., Sippl, C., Ratschbacher, L., ... others (2012). Crustal and uppermost mantle velocity structure along a profile across the Pamir and southern Tien Shan as derived from project TIPAGE wide-angle seismic data. *Geophysical Journal International*, *188*(2), 385–407.

Metzger, S., Schurr, B., Ratschbacher, L., Sudhaus, H., Kufner, S.-K., Schöne, T., ... Bendick, R. (2017). The 2015 Mw7. 2 Sarez strike-slip earthquake in the Pamir interior: Response to the underthrusting of India's western promontory. *Tectonics*, *36*(11), 2407–2421.

Meyer, F. J., & Nicoll, J. B. (2008). Prediction, detection, and correction of faraday rotation in full-polarimetric l-band sar data. *IEEE Transactions on Geoscience and Remote Sensing*, *46*(10), 3076–3086.

Mitchell, E., Fialko, Y., & Brown, K. M. (2013). Temperature dependence of frictional

healing of Westerly granite: experimental observations and numerical simulations. *G-cubed*, *14*, 567–582.

Mitchell, E., Fialko, Y., & Brown, K. M. (2016). Velocity-weakening behavior of Westerly granite at temperature up to 600° C. *J. Geophys. Res.*, *121*, 6932–6946.

Mohadjer, S., Ehlers, T. A., Bendick, R., Stübner, K., & Strube, T. (2016). A Quaternary fault database for central Asia. *Natural Hazards and Earth System Sciences*, *16*(2), 529–542.

Nur, A., & Mavko, J. (1972). Aftershocks caused by pore fluid flow? *Science*, *175*, 885–887.

Okada, Y. (1985). Surface deformations due to shear and tensile faults in a halfspace. *Bull. Seism. Soc. Am.*, *75*, 1135–1154.

Parsons, T. (2005). A hypothesis for delayed dynamic earthquake triggering. *Geophys. Res. Lett.*, *32*, L04302.

Peltzer, G., Rosen, P., Rogez, F., & Hudnut, K. (1998). Poroelastic rebound along the Landers 1992 earthquake surface rupture. *J. Geophys. Res.*, *103*, 30131–30145.

Poliakov, A. B., Dmowska, R., & Rice, J. R. (2002). Dynamic shear rupture interactions with fault bends and off-fault secondary faulting. *J. Geophys. Res.*, *107*, doi:10.1029/2001JB000572.

Pollitz, F. F. (2003). Transient rheology of the uppermost mantle beneath the Mojave Desert, California. *Earth Planet. Sci. Lett.*, *215*, 89–104.

Rice, J. R., & Cleary, M. P. (1976). Some basic stress-diffusion solutions for fluid-saturated elastic porous media with compressible constituents. *Rev. Geophys.*, *14*, 227–241.

Roeloffs, E. (1996). Poroelastic techniques in the study of earthquake-related hydrologic phenomena. *Advances in Geophys.*, *37*, 135–195.

Rosen, P. A., Hensley, S., & Chen, C. (2010). Measurement and mitigation of the ionosphere in l-band interferometric sar data. In *2010 ieee radar conference* (pp. 1459–1463).

Roten, D., Olsen, K., & Day, S. (2017). Off-fault deformations and shallow slip deficit from dynamic rupture simulations with fault zone plasticity. *Geophys. Res. Lett.*, *44*(15), 7733–7742.

Royden, L. H., Burchfiel, B., King, R., Wang, E., Chen, Z., Shen, F., & Liu, Y. (1997). Surface deformation and lower crustal flow in eastern Tibet. *Science*, *276*, 788–790.

Rybicki, K., & Kasahara, K. (1977). A strike-slip fault in a laterally inhomogeneous medium. *Tectonophysics*, *42*, 127–138.

Sandwell, D., Mellors, R., Tong, X., Wei, M., & Wessel, P. (2011). Open radar interferometry software for mapping surface deformation. *Eos Trans. AGU*, *92*(28). doi: 10.1029/2011EO280002

Sangha, S., Peltzer, G., Zhang, A., Meng, L., Liang, C., Lundgren, P., & Fielding, E. (2017). Fault geometry of 2015, Mw7. 2 Murghab, Tajikistan earthquake controls rupture propagation: Insights from InSAR and seismological data. *Earth and Planetary Science Letters*, *462*, 132–141.

Scholz, C. H. (1998). Earthquakes and friction laws. *Nature*, *391*, 37. doi: 10.1038/34097

Schurr, B., Ratschbacher, L., Sippl, C., Gloaguen, R., Yuan, X., & Mechie, J. (2014). Seismotectonics of the Pamir. *Tectonics*, *33*(8), 1501–1518.

Segall, P. (1989, October). Earthquakes triggered by fluid extraction. *Geology*, *17*, 942–946.

Shapiro, N. M., Ritzwoller, M. H., Molnar, P., & Levin, V. (2004). Thinning and flow of Tibetan crust constrained by seismic anisotropy. *Science*, *305*, 233–236.

Shelly, D. R., Peng, Z., Hill, D. P., & Aiken, C. (2011). Triggered creep as a possible mechanism for delayed dynamic triggering of tremor and earthquakes. *Nature Geoscience*, *4*, 384–388.

Simons, M., Fialko, Y., & Rivera, L. (2002). Coseismic deformation from the 1999 Mw 7.1 Hector Mine, California, earthquake as inferred from InSAR and GPS observations. *Bulletin of the Seismological Society of America*, *92*(4), 1390–1402. doi: 10.1785/0120000933

Sippl, C., Schurr, B., Yuan, X., Mechie, J., Schneider, F., Gadoev, M., ... others (2013). Geometry of the Pamir-Hindu Kush intermediate-depth earthquake zone from local seismic data. *Journal of Geophysical Research: Solid Earth*, *118*(4), 1438–1457.

Storchak, D. A., Di Giacomo, D., Bondár, I., Engdahl, E. R., Harris, J., Lee, W. H., ... Bormann, P. (2013). Public release of the ISC–GEM global instrumental earthquake catalogue (1900–2009). *Seismological Research Letters*, *84*(5), 810–815.

Strecker, M., Frisch, W., Hamburger, M., Ratschbacher, L., Semiletkin, S., Zamoruyev, A., & Sturchio, N. (1995). Quaternary deformation in the eastern Pamirs, Tadzhikistan and Kyrgyzstan. *Tectonics*, *14*, 1061–1079.

Takeuchi, C., & Fialko, Y. (2012). Dynamic models of interseismic deformation and stress transfer from plate motion to continental transform faults. *J. Geophys. Res.*, *117*, B05403, doi:10.1029/2011JB009056.

Takeuchi, C., & Fialko, Y. (2013). On the effects of thermally weakened ductile shear zones on postseismic deformation. *J. Geophys. Res.*, *118*, 6295–6310.

Talwani, P., Cobb, J., & Schaeffer, M. (1999). In situ measurements of hydraulic properties of a shear zone in northwestern South Carolina. *J. Geophys. Res.*, *104*, 14993–15003.

Tembe, S., Lockner, D. A., Solum, J. G., Morrow, C. A., Wong, T.-f., & Moore, D. E. (2006). Frictional strength of cuttings and core from safod drillhole phases 1 and 2. *Geophys. Res. Lett.*, *33*.

Tymofyeyeva, E., & Fialko, Y. (2015). Mitigation of atmospheric phase delays in InSAR data, with application to the Eastern California Shear Zone. *J. Geophys. Res.*, *120*, 5952–5963.

Tymofyeyeva, E., Fialko, Y., Jiang, J., Xu, X., Sandwell, D., Bilham, R., ... Moafipoor, S. (2019). Slow slip event on the southern San Andreas fault triggered by the 2017 M_w8.2 Chiapas (Mexico) earthquake. *J. Geophys. Res.*, *124*, 9956–9975.

USGS. (2015). *U.S. Geological Survey. M 7.2 - 104km W of Murghob, Tajikistan.* `https://earthquake.usgs.gov/earthquakes/eventpage/us100044k6/executive*general_summary`. (2015-12-07)

Wallace, R. E., & Morris, H. T. (1986). Characteristics of faults and shear zones in deep mines. *Pure and Applied Geophysics*, *124*(1), 107–125.

Wang, K., & Fialko, Y. (2014). Space geodetic observations and models of postseismic deformation due to the 2005 M7.6 Kashmir (Pakistan) earthquake. *J. Geophys. Res.*, *119*(9), 7306–7318.

Wang, K., & Fialko, Y. (2015). Slip model of the 2015 M_w 7.8 Gorkha (Nepal) earthquake from inversions of ALOS-2 and GPS data. *Geophys. Res. Lett.*, *42*, 7452–7458. doi: 10.1002/2015GL065201

Wang, K., & Fialko, Y. (2018). Observations and modeling of co- and postseismic deformation due to the 2015 M_w 7.8 Gorkha (Nepal) earthquake. *J. Geophys. Res.*, *123*(1), 761–779.

Wang, R., Lorenzo-Martin, F., & Roth, F. (2006). PSGRN/PSCMP-a new code for calculating co- and post-seismic deformation, geoid and gravity changes based on the viscoelastic-gravitational dislocation theory. *Comp. Geosci.*, *32*, 527–541.

Wang, R., Martin, F., & Roth, F. (2003). Computation of deformation induced by earthquakes in a multi-layered elastic crust - FORTRAN programs EDGRN/EDCMP. *Comp. Geosci.*, *29*, 195–207.

Wang, Y., Lin, Y.-N. N., Simons, M., & Tun, S. T. (2014). Shallow rupture of the 2011 Tarlay earthquake (Mw 6.8), eastern Myanmar. *Bull. Seism. Soc. Am.*, *104*, 2904–2914.

Wessel, P., Smith, W. H. F., Scharroo, R., Luis, J., & Wobbe, F. (2013). Generic Mapping Tools: Improved Version Released. *Eos, Trans. AGU*, *94*(45), 409–410. Retrieved from `http://onlinelibrary.wiley.com/doi/10.1002/2013EO450001/abstract` doi: 10.1002/2013EO450001

Yamashita, T., & Umeda, Y. (1994). Earthquake rupture complexity due to dynamic nucleation and interaction of subsidiary faults. *Pure Appl. Geophys.*, *143*.

Zhao, B., Bürgmann, R., Wang, D., Tan, K., Du, R., & Zhang, R. (2017). Dominant controls of downdip afterslip and viscous relaxation on the postseismic displacements following the Mw7.9 Gorkha, Nepal, earthquake. *J. Geophys. Res.*, *122*, 8376–8401.

Zhao, D., Qu, C., Bürgmann, R., Gong, W., & Shan, X. (2021). Relaxation of Ti-

betan Lower Crust and Afterslip Driven by the 2001 Mw7.8 Kokoxili, China, Earthquake Constrained by a Decade of Geodetic Measurements. *J. Geophys. Res.*, *126*, e2020JB021314.

Zhao, W.-L., & Morgan, W. J. (1987). Injection of Indian crust into Tibetan lower crust: A two-dimensional finite element model study. *Tectonics*, *6*(4), 489–504.

Zinke, R., Hollingsworth, J., & Dolan, J. F. (2014). Surface slip and off-fault deformation patterns in the 2013 Mw 7.7 Balochistan, Pakistan earthquake: Implications for controls on the distribution of near-surface coseismic slip. *Geochemistry, Geophysics, Geosystems*, *15*(12), 5034–5050.

Ziv, A., & Rubin, A. (2000). Static stress transfer and earthquake triggering: No lower threshold in sight? *J. Geophys. Res.*, *105*, 13631–13642.

Zubovich, A., Schöne, T., Metzger, S., Mosienko, O., Mukhamediev, S., Sharshebaev, A., & Zech, C. (2016). Tectonic interaction between the Pamir and Tien Shan observed by GPS. *Tectonics*, *35*, 283–292.

Zubovich, A., Wang, X.-q., Scherba, Y. G., Schelochkov, G. G., Reilinger, R., Reigber, C., ... others (2010). GPS velocity field for the Tien Shan and surrounding regions. *Tectonics*, *29*, TC6014.